MMath Project

Properties of Tracer Particles in Turbulence

Author:
Anthony Murphy

Supervisor:
Prof. Carlo Barenghi

May 1, 2014

Abstract

The results of the direct numerical simulations that model the trajectories of 500 heavy, neutrally buoyant and light tracer particles in turbulence are presented in two-dimensions. It has been validated that heavy tracers preferentially concentrate into areas of low vorticity or high strain, neutrally buoyant tracers act chaotically and can take trajectories simply not allowed by the surrounding fluid parcels of the same density, and light particles can easily get trapped in vortex trajectories. Upon considering the normalised velocity and acceleration components of these tracer particles, it is observed that the normalised velocity probability density function (PDF) in each case is near Gaussian, but best fits in the tails of these distributions belong to the exponential distribution of varying steepness, where flatter distributions occur when the Stokes number, $St \ll 1$, observed in light cases. The normalised acceleration PDFs are strictly non Gaussian with exponential tails, where flatter distributions again occur when $St \ll 1$.

Contents

Chapter 1

Introduction

For the best part of two centuries, Newtonian mathematics attempted to define the world we know. Following clearly constructed rules reliant upon cause and effect seemingly made our surroundings predictable, almost mechanical and thusly controllable. Mathematics was king, answering all questions that nature could offer. However, towards the middle of the 20^{th} century mathematics was dethroned. It became impossible to find the answers to a new, anti-Laplacian perception that duly presented unstable, chaotic and turbulent problems. This lead to the current position in which modern applied mathematics is placed today, where attempts are made to pick apart and rebuild the unpredictable nature in which it has been presented. This report shall consider elements of turbulence, where current research remains focused upon building on the pioneering work of Kolmogorov, but more specifically the problem presented by impurities in turbulent fluids. The method in which this shall be considered is by the use of tracer particles, which throughout recent history could of been utilised to model the release of chlorofluorocarbons (CFCs) into the atmosphere in the mid 1980s, the trajectories taken by dust particles or pieces of abraded metal in jet engines or the motion of hot gases in accretion disks surrounding binary stars. These widespread examples, as well as the fundamental academic interest surrounding the topic have assisted in propelling this sector towards the forefront of fluid dynamical research, as highlighted by the vast quantity of talk time regarding tracer particles at the recent *European Turbulence Conference 14* in Lyon.

In light of this interest, the aim of this report is to gain a better understanding of the behaviour of the different types of tracer particles that are subdued in a computed turbulent fluid, as well as considering particular properties in which turbulence may possess itself. The breakdown of how this is attempted is as follows.

In chapter 2, the preliminary ideas and thoughts are described, providing a foundation layer. This chapter shall outline the forces that have been considered in deriving a model to describe the motion of a small, spherical tracer particle in a fluid whilst stating the relevant assumptions that have been made. In addition to this, some conventions that are frequently used throughout this report shall be introduced here.

In chapter 3, the fundamental results are presented that describe the application of the derived model, compared to a simplified model, for the cases of *heavy*, *neutrally buoyant* and *light* particles in mathematically viable, Eulerien fluids. Following on from this, a comparison is made to recent academic resources, resulting in an analysis of the

trajectories that the tracers can take. It is observed that different tracer particles seek areas within the fluid that can be described by different mathematical quantities, and so it is possible to categorise their trajectories.

In chapter 4, the method in which a turbulent fluid is simulated is discussed. The vortex points model lends much of its derivation to the computation of quantum turbulence, and the considerations taken into account when constructing this model are tested to examine its performance. In addition to this, consideration is given to looking at the turbulent fluid from a statistical perspective. The probability density functions (PDFs) are calculated for the x and y components of the velocity and acceleration of the fluid elements, where it is observed that there are strictly non-Gaussian tendencies.

In chapter 5, the elements and results that have been derived in chapters 2-4 are combined. The trajectory and motion PDFs are considered for the different types of tracer particle in the aforementioned simulated turbulent fluid.

It should be noted that all numerical computations and figures have been computed in `Matlab` and produced in full by the author.

Chapter 2

Preliminaries

In this chapter the general methods and equations that are considered throughout this report are outlined, in addition to discussing the specific considerations and conventions that have been used throughout. This is where the problem at hand is addressed.

First of all, the equation of motion for a tracer particle of radial length r and density ρ_p, placed in a surrounding fluid of density ρ_f that is considered viscous with non-uniform velocity is constructed. As derived from first principles by Maxey and J.Riley (1983) and discussed by Poole et al. (2005), whilst ignoring superfluid and lift components, the equation of motion is defined as

$$\rho_p \vartheta \frac{d\mathbf{u}_p}{dt} = \mathbf{F}^{(\mathrm{g})} + \mathbf{F}^{(\mathrm{d})} + \mathbf{F}^{(\mathrm{i})} + \mathbf{F}^{(\mathrm{a})} + \mathbf{F}^{(\mathrm{B})} + \mathbf{F}^{(\mathrm{F})}, \tag{2.1}$$

where $\vartheta, \mathbf{u}_p$ denotes the tracer's volume and velocity respectively. It can be seen that Newton's second law has been applied here, where the resultant force acting on the tracer is equal to the mass of the tracer ($\rho_p \vartheta$) multiplied by the tracer's acceleration (the first time derivative of the tracer's velocity). It should be noted that the model is considered using the standard right handed, cartesian co-ordinate system. Each force will now be reviewed separately.

2.1 $\mathbf{F}^{(\mathrm{g})}$: Gravitational Force

Firstly, consideration will be given to the acceleration force exerted on the particle due to gravity, which acts strictly along the z-axis from positive to negative. This term determines whether the tracer will sink to the base of the container or float to the surface of the fluid. The gravitational force can be defined as

$$\mathbf{F}^{(\mathrm{g})} = \vartheta(\rho_p - \rho_f)\mathbf{g} = \vartheta(\rho_p - \rho_f)g\hat{\mathbf{z}}, \tag{2.2}$$

where $g = -9.81\mathrm{ms}^{-2}$ is the gravitational acceleration. Relating this to expected results, if the particle is deemed heavy, where $\rho_p > \rho_f$, it is observed that $\mathbf{F}^{(\mathrm{g})} < 0$, contributing to the particle travelling to the bottom of the container. Whereas in the event of a light tracer particle, when $\rho_p < \rho_f$, it follows that $\mathbf{F}^{(\mathrm{g})} > 0$, assisting in transporting the particle to the surface of the fluid. From this it can be gathered that the velocity at which the tracer will sink or float is proportional to the magnitude of the difference between the densities of the tracer and fluid.

2.2 $\mathbf{F}^{(\mathrm{d})}$: Viscous Drag Force

Next the viscous drag force is considered, which offers a resistance to the motion of the tracer. This term has been constructed such that Stokes' drag (also known as Stokes' law of resistance) acts on the tracer particle, in which it is assumed that the tracer is small and spherical, whilst subdued in a continuous fluid. The viscous drag force is defined as

$$\mathbf{F}^{(\mathrm{d})} = 6\pi r \mu_f (\mathbf{u}_f - \mathbf{u}_p), \tag{2.3}$$

where μ_f, $\mathbf{u}_f$ denotes the dynamic viscosity and velocity of the fluid respectively. For consistency throughout, tracer particles are considered initially at rest within the fluid. As the tracer particle accelerates due to the velocity field induced by the fluid, the conjecture can be formed that the velocity of the tracer can not be greater than the velocity of the fluid parcel local to the position of the tracer. In this limit, when $\mathbf{u}_p \to \mathbf{u}_f$, $\mathbf{F}^{(\mathrm{d})} \to 0$ implying viscous drag effects become negligible and the tracer particle shall move as one with the fluid.

2.3 $\mathbf{F}^{(\mathrm{i})}$: Inertial Force

Now the effects of the inertial force that acts on the tracer particle due to the acceleration of the carrier fluid are examined. This term describes how the velocity of the small parcel of fluid, local to the position of the tracer particle, evolves at each time interval. It is given by

$$\mathbf{F}^{(\mathrm{i})} = \rho_f \vartheta \frac{D\mathbf{u}_f}{Dt}, \tag{2.4}$$

where the material derivative has been used as the fluid is observed on a mesoscopic level. This convention is used as it is inconvenient to consider the fluid as a collection of particles, in which the spaces in-between the fluid molecules would have to be accounted for, thus ignoring the continuum hypothesis. The fluid is not observed as a whole either, as shall be seen in the mathematically viable, test fluids and also in turbulence. This is because different fluid parcels will move with different velocities dependent on their spatial position, which is not accounted for on the macroscopic level. Recall that the material derivative of the velocity field generated by the fluid is defined as

$$\frac{D\mathbf{u}_f}{Dt} = \frac{\partial \mathbf{u}_f}{\partial t} + \mathbf{u}_f \cdot (\nabla \mathbf{u}_f)\,. \tag{2.5}$$

2.4 $\mathbf{F}^{(\mathrm{a})}$: Added Mass Force

The added mass force accounts for the inertia added to the system because of the accelerating (or decelerating) tracer, which upon motion causes a small displacement of fluid. This term has been included because the fluid and the tracer particle cannot occupy the same physical space at the same time, leading to the aforementioned displacement of fluid. It is defined as

$$\mathbf{F}^{(\mathrm{a})} = C\rho_f \vartheta \left(\frac{D\mathbf{u}_f}{Dt} - \frac{d\mathbf{u}_p}{dt} \right), \tag{2.6}$$

where C is the drag co-efficient of the tracer particle, which is determined by the cross sectional area of the tracer particle perpendicular to the motion of the fluid.

2.5 $\mathbf{F}^{(\mathrm{B})}$: Basset History Force

The Basset history force acts on the tracer particle due to the lagging boundary layer development associated with the change in velocity of the tracer as it approaches a boundary. This term accounts for viscous effects whilst addressing the temporal delay in the boundary development. As typical in reports of this type, due to the practical difficulties in implementing this force in direct numerical simulations, it will be neglected. In order to ignore this term, it is assumed that the particle relaxation time, τ_p, is smaller than than the characteristic time of the fluid, τ_f. In turbulence, τ_f is given by the turnover time of the smallest eddies in the velocity field.

2.6 $\mathbf{F}^{(\mathrm{F})}$: Fáxen Correction Force

The Fáxen correction force is an amendment to Stokes' law, which as discussed previously the tracer particle follows. Stokes' law states the flow surrounding the tracer particle follows the inverse of the particle relaxation time, given by

$$\frac{1}{\tau_p} = \frac{9\mu_f}{2r^2\rho_0},\ \rho_0 = \rho_p + \frac{1}{2}\rho_f. \tag{2.7}$$

In comparison to the standard definition of Stokes' law, the equation above contains a weighted contribution of the density of the fluid defined by ρ_0, this occurs due to the implementation of $\mathbf{F}^{(\mathrm{a})}$. The Fáxen correction becomes valid when the tracer particle approaches the boundary of the fluid. In a turbulent flow, this force is ignorable under the assumption that the size of the tracer particle is smaller than the Kolmogorov dissipation length scale ($\eta = (\nu^3/\epsilon)^{1/4}$, where ν = kinematic viscosity of the fluid and ϵ = average rate of dissipation of turbulence kinetic energy per unit mass).

2.7 Combing Terms

Upon substituting the aforementioned forces back into equation (2.1), the general equation describing the motion of a small, spherical tracer particle can be defined. It is given by

$$\begin{aligned}\rho_p\vartheta\frac{d\mathbf{u}_p}{dt} =& \vartheta(\rho_p - \rho_f)g\hat{\mathbf{z}} + 6\pi r\mu_f(\mathbf{u}_f - \mathbf{u}_p) \\ &+ \rho_f\vartheta\frac{D\mathbf{u}_f}{Dt} + C\rho_f\vartheta\left(\frac{D\mathbf{u}_f}{Dt} - \frac{d\mathbf{u}_p}{dt}\right).\end{aligned} \tag{2.8}$$

From this typical values for each constant to replicate laboratory like conditions can be considered. Firstly the characteristics of the fluid shall be examined. For consistency throughout, the constants that relate to the fluid are chosen to replicate water, thus $\rho_f = 1\ \mathrm{gcm}^{-3} = 1000\ \mathrm{kgm}^{-3}$ and $\mu_f = 0.001002\ \mathrm{Pa}\cdot\mathrm{s}$. Now for the geometry of the particle; as it is required to be spherical and small, it is concluded that $\vartheta = (4\pi r^3)/3$,

$C = 1/2$ and a radial length for the particle of $r = 2.5$ mm $= 0.0025$ m should suffice and remain valid under the previously stated assumptions.

2.8 Two-Dimensional Model

The general equation of motion is now simplified such that it is considered in the x-y plane only, ignoring the gravitational term. This will be often referred back to, the fundamental equation that will be consistently solved throughout this report for the cases of *heavy*, *neutrally buoyant* and *light* particles. In this two dimensional model, equation (2.8) can be written as

$$\frac{d\mathbf{u}_p}{dt} = \frac{9\mu_f}{2r^2\rho_0}(\mathbf{u}_f - \mathbf{u}_p) + \frac{3\rho_f}{2\rho_0}\frac{D\mathbf{u}_f}{Dt}, \tag{2.9}$$

where the coefficients of the slip velocity $(\mathbf{u}_f - \mathbf{u}_p)$ and the material derivative term are constants, which will vary upon choice of particle density. Under this observation, the constants A and B are introduced such that

$$A = \frac{9\mu_f}{2r^2\rho_0}, \qquad B = \frac{3\rho_f}{2\rho_0}, \tag{2.10}$$

leading to the system of equations given by

$$\begin{aligned} \frac{d\mathbf{u}_p}{dt} &= A(\mathbf{u}_f(\mathbf{r}_p, t) - \mathbf{u}_p) + B\frac{D\mathbf{u}_f(\mathbf{r}_p, t)}{Dt}, \\ \frac{d\mathbf{r}_p}{dt} &= \mathbf{u}_p. \end{aligned} \tag{2.11}$$

Three points should be noted. Firstly, the velocity of the fluid is evaluated at the position of the particle at each time interval, i.e. $\mathbf{u}_f = \mathbf{u}_f(\mathbf{r}_p, t)$, whereas the velocity of the particle is simply split into x and y components, $\mathbf{u}_p = (u_p, v_p)$. Secondly, in deriving this model *one way coupling* has been assumed, this means the fluid induces it's velocity field onto the particle but does not receive feedback, implying the particle in no way affects the motion of the fluid. Finally, it has been assumed that the Reynolds number, Re, based upon the relative velocities between the tracer particle and fluid is small, that is $Re \ll 1$. This means the fluids motion is relatively smooth, and so the tracer particle will act as it is expected to. From this point, the system of equations given by equation (2.11) will be referred to as model 1.

2.9 Test Fluids

Before a turbulent fluid is considered, a comprehensive evaluation of the behaviour of the different tracers in simple, mathematically viable fluids is sought. In order to fulfil this requirement, the trajectories of the different tracers in two different test fluids are simulated. And so this report shall consider (a), the solid body rotating fluid and it's reciprocal (b), a vortex. These fluids have been selected in order to observe whether the trajectories of the different tracers tend towards different locations, thus making it

possible to diagnose a mathematical quantity to describe their motion. The velocity fields for (a) and (b) in polar co-ordinates, are respectively given by

$$\begin{aligned} &\text{(a): } \mathbf{u}_f\left(u_r, u_\theta\right) = \left(0, \kappa r\right), \\ &\text{(b): } \mathbf{u}_f\left(u_r, u_\theta\right) = \left(0, \frac{\Gamma}{2\pi r}\right), \end{aligned} \tag{2.12}$$

where Γ and κ are constants, r denotes the radial length away from the origin the fluid parcels are located and u_r, u_θ denotes the radial and angular velocity components respectively. Figure 2.1 highlights the differences in the velocity profiles, where the

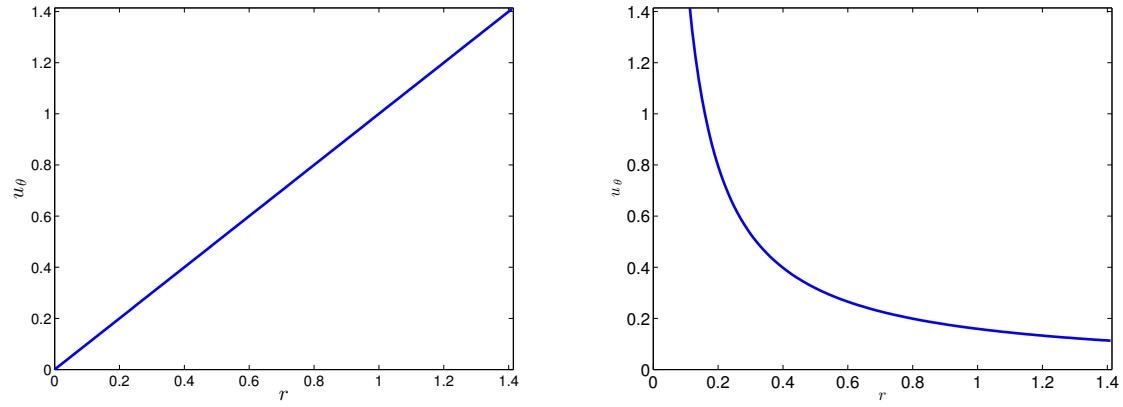

(a) Solid body rotating

(b) Vortex

Figure 2.1: A plot showing how the angular velocity of the fluids changes due to the radial distance away from the centre of the vortex the fluid particles are.

angular velocity of both fluids differs due to the radial distance from the origin the fluid parcel is located. In (a), the solid body rotating fluid, it is seen that the radial velocity of the fluid increases linearly as r increases, with the area of maximum angular velocity being located towards the edges of the confined box. Compare this to (b), the vortex, where in the limit of $r \to 0$, $\mathbf{u}_f \to \infty$, exposing a singularity point. Here it must be stressed that the fluid elements local to the singularity point will be confined to an area of zero velocity, to avoid $\mathbf{r}_p \to \infty$.

In order to use model 1, the fluid velocity fields must be converted from polar into cartesian co-ordinates. Upon calculating this simple transformation, equation (2.12) becomes

$$\begin{aligned} &\text{(a): } \mathbf{u}_f\left(u, v\right) = \left(-\kappa y, \kappa x\right), \\ &\text{(b): } \mathbf{u}_f\left(u, v\right) = \left(\frac{-\Gamma y}{2\pi\left(x^2+y^2\right)}, \frac{\Gamma x}{2\pi\left(x^2+y^2\right)}\right), \end{aligned} \tag{2.13}$$

where u and v denote the x and y components of the fluid velocity respectively. For consistency throughout the initial testing, $\Gamma = \kappa = 1/2$.

2.10 Method of Solving

Throughout, this report will be using the 4^{th} *order Runge-Kutta* method for solving the system of ordinary differential equations given by model 1, presented by Cheney and

Kincaid (2008). This method was designed by *Carl Runge* and *Wilhelm Kutta* with the idea of imitating a Taylor Series expansion without the further differentiation (to whatever degree of accuracy) of the original ordinary differential equation. The iterative procedure for this method, for the initial value problem of

$$\begin{aligned} \frac{dx}{dt} &= u(x, y, t),\ x(0) = x_0, \\ \frac{dy}{dt} &= v(x, y, t),\ y(0) = y_0, \end{aligned} \tag{2.14}$$

goes by

$$\begin{aligned} x_{n+1} &= x_n + \frac{h}{6}\left(k_1 + 2k_2 + 2k_3 + k_4\right), \\ y_{n+1} &= y_n + \frac{h}{6}\left(l_1 + 2l_2 + 2l_3 + l_4\right), \\ t_{n+1} &= t_n + h, \end{aligned} \tag{2.15}$$

where

$$\begin{cases} k_1 = u(x_n, y_n, t_n) \\ k_2 = u(x_n + \frac{h}{2}k_1, y_n + \frac{h}{2}l_1, t_n + \frac{h}{2}) \\ k_3 = u(x_n + \frac{h}{2}k_2, y_n + \frac{h}{2}l_2, t_n + \frac{h}{2}) \\ k_4 = u(x_n + k_3, y_n + l_3, t_n + h) \end{cases}, \begin{cases} l_1 = v(x_n, y_n, t_n) \\ l_2 = v(x_n + \frac{h}{2}k_1, y_n + \frac{h}{2}l_1, t_n + \frac{h}{2}) \\ l_3 = v(x_n + \frac{h}{2}k_2, y_n + \frac{h}{2}l_2, t_n + \frac{h}{2}) \\ l_4 = v(x_n + k_3, y_n + l_3, t_n + h) \end{cases}, \tag{2.16}$$

and h is the step size. It can be seen that deriving each value for x_{n+1} and y_{n+1} requires evaluating the functions u and v four times within each time step, which for consistency throughout this report, will be set as $h = 0.001s$. This agrees with the formula of a Taylor expansion up to and including the term of order h^4 and so the total error accumulated is of order $\mathcal{O}(h^4)$.

Chapter 3

Comparison to Previous Publications

This chapter will solve the system of equations that were derived in chapter 2 that defines the trajectory of a tracer particle, whilst subdued in both test fluids. In doing this, model 1's performance will be analysed compared to a simplified model that is often used to describe heavy particles suspended in turbulent fluids. This shows the impact caused by the omission of some of the terms discussed previously and why it is fundamental that they are considered in non-heavy cases. Following on from this, the raw principles surrounding the characteristics of the tracer's trajectories that are gathered from the test fluids are evolved and a more complex flow is considered. These results shall be compared to those gathered in previous literature.

3.1 A Simplified Model

Initially, the compromised model must be examined, this has been used previously when describing the motion of tracer particles that are much heavier than the surrounding fluid, as used by Squires and Eaton (1991) and Bec et al. (2006). This simple model is defined as

$$\begin{aligned} \frac{d\mathbf{u}_p}{dt} &= \alpha(\mathbf{u}_f(\mathbf{r}_p, t) - \mathbf{u}_p), \\ \frac{d\mathbf{r}_p}{dt} &= \mathbf{u}_p, \end{aligned} \tag{3.1}$$

where the notation has been altered such that it is consistent to that defined in the previous chapter. The co-efficient α is defined as the inverse of the particle response time, τ_p, where it has been assumed that the fluid flow around the tracer particle follows Stokes' law of resistance, given by

$$\alpha = \frac{1}{\tau_p} = \frac{18\mu_f}{\rho_p(2r)^2} = \frac{9\mu_f}{2r^2\rho_p}. \tag{3.2}$$

It is noted that the model is appropriate under the assumption that $Re \ll 1$ and the particle size is considered to be smaller than the smallest length scale of the fluid flow. Hereafter, this simplified model will be termed 'model 2'.

There are two major differences between model 1 and model 2. Firstly, it can be observed that model 2 has only taken into account the sling velocity term. The remaining terms have been omitted as they were deemed negligible in the limiting case when $\rho_p \gg \rho_f$. For example, when applied previously in academic resources, Squires and Eaton (1991) used the model because they intended to examine the transport and mixing properties of heavy particles in turbulent flow fields, whereas Bec et al. (2006) presented the acceleration statistics of heavy particles in turbulent flow fields. As can be seen, there was no comparison to the different types of tracer, as the density itself was arbitrary. Secondly, a difference can be seen in the coefficient of the slip velocities in both models, A and α. Here it can be seen that the density term in A involves a weighted contribution from the fluid, whereas α does not. This will impact τ_p in each case and also the Stokes number, defined as

$$St = \frac{\tau_p}{\tau_f}, \tag{3.3}$$

where τ_f denotes the characteristic time of the fluid. The Stokes number describes the behaviour of particles suspended in a fluid. When $St \ll 1$, the tracer will follow the streamlines of the fluid incredibly closely, whereas when $St \gg 1$ the particles will act unpredictably and against the direction of fluid motion. As the models produce different values of τ_p, it can be expected that the trajectories of the tracers will be different in the test fluids.

Now a comparison can be drawn between these two models, and the importance of the inclusion of the material derivative term in model 1 can be highlighted.

3.2 A Heavy Particle

Firstly, the trajectory taken by a tracer that is heavier than the surrounding fluid, where $\rho_f < \rho_p = 10500$ kgm^{-3} is considered. ρ_p has been chosen such that it simulates

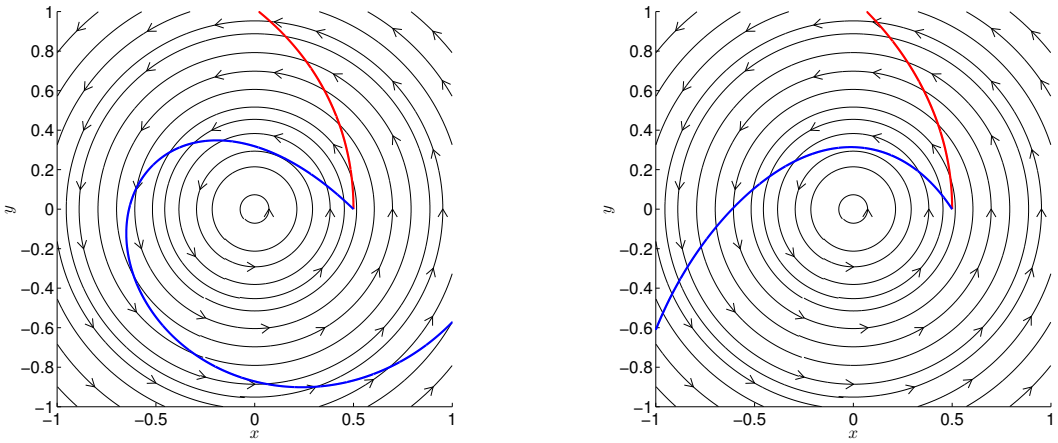

(a) Solid body rotating

(b) Vortex

Figure 3.1: The heavy tracer's trajectories, superimposed over the fluid streamlines. The blue and red lines corresponds to model 1 and model 2 respectively. Starting position in each case is (1/2,0).

a silver tracer particle. Comparing the two equations of motion shows that model 2 behaves well in this limit. The coefficients of the slip velocities are similar, such that $\alpha \approx A \ll 1$. This is an expected result; as α and A denote τ_p^{-1}, it follows that $\tau_p \gg 1$. In this limit, $St \gg 1$ due to the Eulerien nature of both fluids and so the particles following both models are expected to detach from the streamlines of the fluid. This has been illustrated in figure 3.1, where the trajectories of the particles following both models act away from fluid streamlines of both fluids immediately. It can also be noted that $B \approx 2A \ll 1$, implying the effect of the material derivative term, that attempts to draw the particle towards the centre of the container, is small and does not dominate model 1. This effect is also viewed in figure 3.1, where although the trajectory of the particle initially gets drawn closer towards the origin in both test fluids, the particle eventually seeks to locate itself away from the centre of the fluid. This characteristic is consistent to the entire trajectory of the particle following model 2 in both fluids.

3.3 A Neutrally Buoyant Particle

The trajectory taken by a tracer that is of the same density of the surrounding fluid, where $\rho_f = \rho_p = 1000\ \mathrm{kgm}^{-3}$, shall be examined. This is of interest as it is shown that neutrally buoyant tracers do not follow the same trajectories as real fluid elements. Considering the equations of motion, some important differences separating the models can start to be seen. It follows that $\alpha \approx 3/4$ whereas $A \approx 1/2$ and $B = 1$. As τ_p is

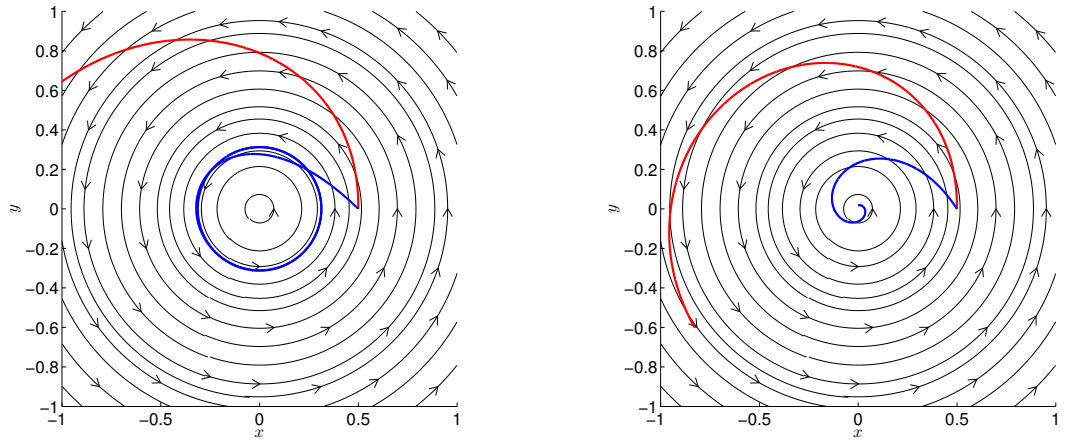

(a) Solid body rotating

(b) Vortex

Figure 3.2: The neutrally buoyant tracer's trajectories, superimposed over the fluid streamlines. The blue and red lines corresponds to model 1 and model 2 respectively. Starting position in each case is (1/2,0).

different in each model but greater than 1, it is expected the tracer should detach from the fluid streamlines as the particle's response time is too large to react to changes in fluid velocity. However, in model 1 there is now a greater contribution from the material derivative term, thus the expectation of completely different particle trajectories between models. As shown in figure 3.2, the particles that follow model 1 are initially inclined to travel towards the centre as highlighted by both blue trajectories, caused

by the inclusion of the material derivative term. These trajectories are now seen to be different due to the choice of fluid. In the solid body rotating fluid, it is observed that as $\mathbf{u}_p \to \mathbf{u}_f$, the particle is allowed to settle into the streamlines of the fluid as equilibrium is met in the model, where the particle's trajectory becomes proper for a real fluid parcel. However, in the vortex the particle can never achieve this limit, as $\mathbf{u}_f$ is unbounded and so equilibrium can never be met. This means the particle is not able to settle into the streamlines of the fluid as it will continually attempt to travel with increasing velocity, thus it's trajectory continues to travel towards the region containing the singularity point. The flaws of model 2 are also highlighted. Due to the absence of the material derivative term, the trajectories in which the particle can take are now limited and dependent entirely on St. It is seen that as $St > 1$, the particles in both fluids detach from the fluid streamlines and travel against expected results.

3.4 A Light Particle

Finally, the trajectory of a tracer that is lighter than the surrounding fluid, where $\rho_f > \rho_p = 1.2\ \mathrm{kgm}^{-3}$, shall be observed. ρ_p has been chosen such that it models a hollow tracer particle. Comparing the equations of motion draws attention to the major flaws in model 2 when used in non-heavy cases. It is seen that $\alpha \gg 1$, $A \approx 3/2$

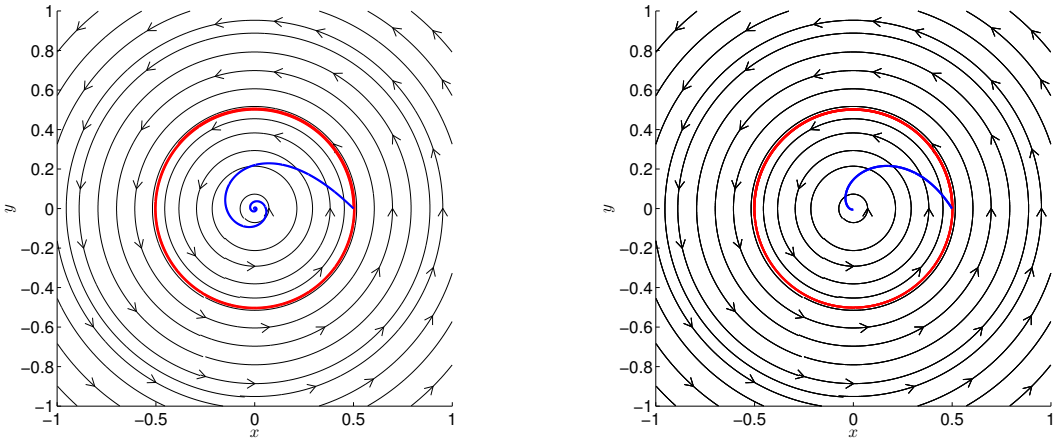

(a) Solid body rotating

(b) Vortex

Figure 3.3: The light tracer's trajectories, superimposed over the fluid streamlines. The blue and red lines corresponds to model 1 and model 2 respectively. Starting position in each case is (1/2,0).

and $B \approx 3$. In this case, there are major differences between τ_p of both models, thus affecting St and the trajectory of the particle in each case. It is expected that the tracer following model 2 should follow fluid streamlines incredibly closely because $\tau_p \ll 1$, thus $St \ll 1$, however the tracer following model 1 will act differently due to the dominance of the material derivative term. In this limit

$$\frac{d\mathbf{u}_p}{dt} \approx 3\frac{D\mathbf{u}_f(\mathbf{r}_p, t)}{Dt}, \tag{3.4}$$

thus the tracer should travel towards the centre of the fluid, as the material derivative term acts like a pressure. These explanations have been illustrated in figure 3.3, where

in model 1 and in both fluids, the particle gets drawn towards the centre of the fluid, appearing trapped. Whereas the trajectory of the light particle in model 2 follows the streamlines of both fluids incredibly closely, travelling as if a fluid element.

The results from the light and neutrally buoyant tracers has allowed us to witness the flaws of model 2, where the absence of crucial terms allows the tracer particles to act unexpectedly. However it has been seen that model 1 acts well in all scenarios, with a common feature being the material derivative term is accounted for twice the slip velocity ($B \approx 2A$), and so the trajectory of the particle can be deemed reliant upon the characteristic time of the particle.

3.5 Many Tracer Particles

The raw principles regarding the trajectories of different tracers can now be evolved, and consideration is given to quantifying the behaviour of many tracer particles in a more interesting fluid. These results are compared to those previously gathered in academic research. It is assumed that the concentration of tracer particles is small enough such that there are no particle-particle interactions, and the motion of the tracer particle leaves the fluid undisturbed. Following from Babiano et al. (2000), who showed in the case of a neutrally buoyant spherical particle that tracers can take trajectories impossible for fluid elements, they used the periodic stream function

$$\psi(x, y, t) = P \cos(x + Q \sin \omega t) \cos y, \tag{3.5}$$

where the fluid velocity field is defined by

$$\mathbf{u}_f = \left(\frac{\partial \psi}{\partial y}, -\frac{\partial \psi}{\partial x} \right). \tag{3.6}$$

In this section, and for consistency, the fluid is considered to be *steady*, that is it has no time dependence and as such, $Q = 0$. The fluid is periodic and contains fixed vortices separated by a distance πm with circulation that alternates between $\pm P$. A periodic boundary condition is introduced that acts toroidally, meaning if a tracer leaves the box out of the left or bottom, it re-enters the box on the right or top and vice versa. The length of the edges of the square box is 2πm, ranging between $[0, 2\pi]$.

Having asserted that model 1 behaves better in all scenarios, this is the model used hereafter. 500 independent tracer particles are now considered, and they are initially distributed such that the x and y co-ordinates of the position of the particle, $x_p, y_p \sim U(0, 2\pi)$. Also, the tracers are initially at rest within the fluid and $P = 1/5$.

3.5.1 Heavy

Initially, heavy particles are examined. In the study of Squires and Eaton (1991), they agreed with Maxey (1987), and found that heavy particles *preferentially concentrate*. This phenomena has been known for some time and is still a very active research area, with experimental evidence provided by Saw et al. (2008) and Monchaux et al. (2010). These publications conclude that the heavy particle's motion seeks areas of low vorticity or high strain. In figure (3.4) it is shown that as time progresses, the tracer particles

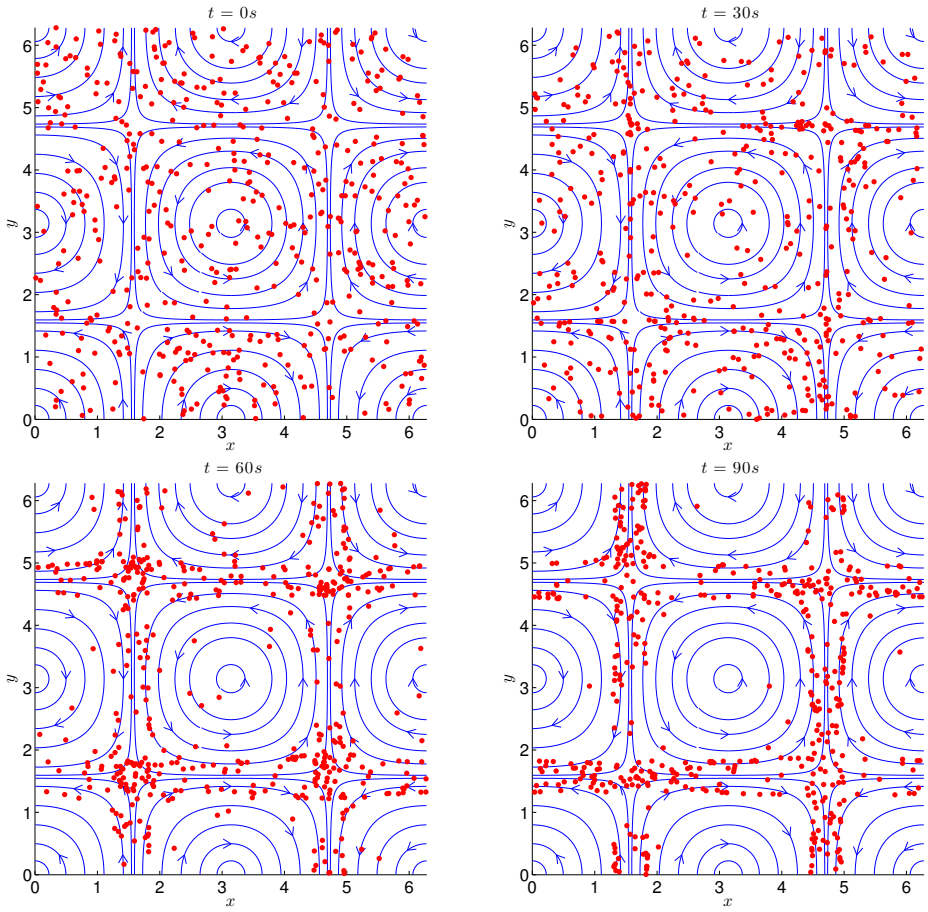

Figure 3.4: A plot showing the evolution of the position of the heavy tracer particles at different time intervals. Here $t = 0, 30, 60, 90s$

attempt to position themselves in between vortex trajectories showing a preference to this region. Recall that the vorticity ($\boldsymbol{\omega}$) and strain ($e_{ij}, i, j \in x, y, z$) in the x-y plane are defined by

$$\boldsymbol{\omega} = \left(\frac{\partial v}{\partial x} - \frac{\partial u}{\partial y}\right)\hat{\mathbf{z}}, \; e_{xy} = \left(\frac{\partial v}{\partial x} + \frac{\partial u}{\partial y}\right)\hat{\mathbf{z}},$$

and upon inputting the velocity components of the fluid yields

$$\boldsymbol{\omega} = 2\cos x \cos y\hat{\mathbf{z}}, \; e_{xy} = 0.$$

Considering x and y values to minimise the magnitude of the vorticity vector, it is seen that this is achieved when x or $y = \pi/2 + n\pi$, $n = 0, 1$. Although strain-less, the areas in between vortices in which the tracers travel towards in figure 3.4 correspond to the areas where the vorticity is at its lowest, showing this preferential concentration and validating the previous theoretical and experimental work. It can also be established, as shown by Squires and Eaton (1991), that preferential concentration in fact inhibits the mixing properties of the tracer particles, thereby reducing the area in which heavy tracers are likely to be found.

3.5.2 Neutrally Buoyant

Many neutrally buoyant particles are discussed by Sergeev et al. (2006) and Babiano et al. (2000), they discussed the trajectories of solid that neutrally buoyant tracers are unstable and not allowed by fluid elements. It is shown in figure 3.5 that initially, the

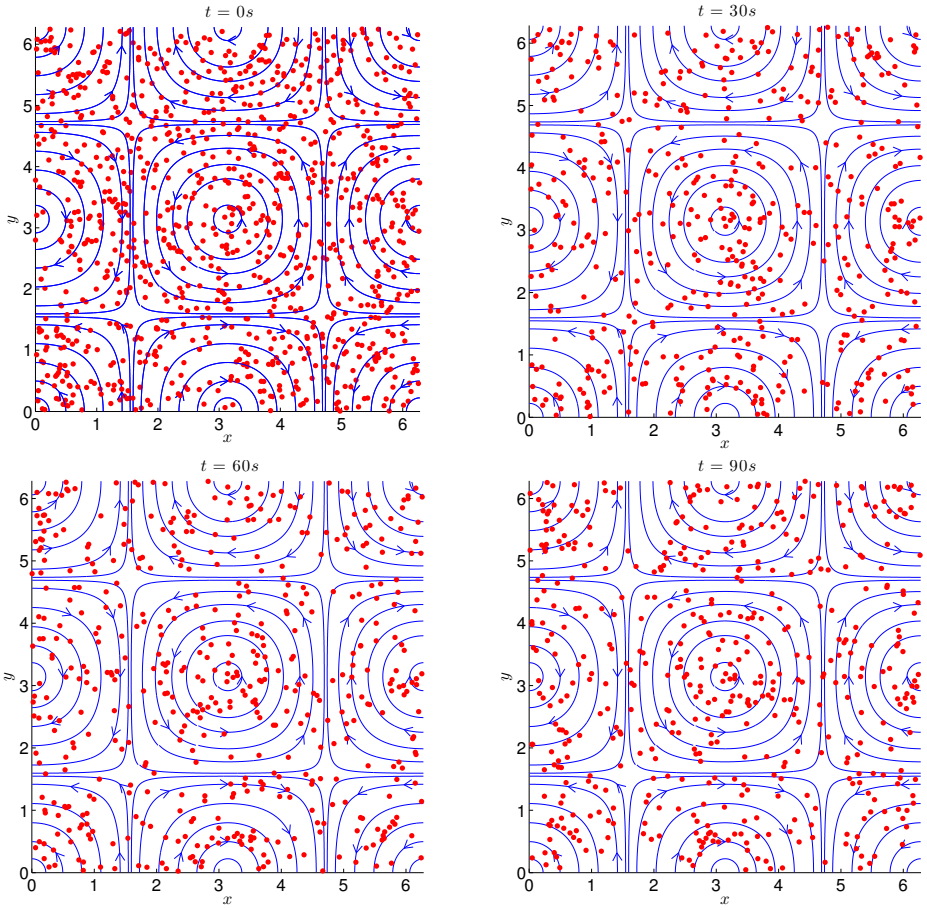

Figure 3.5: A plot showing the evolution of the position of neutrally buoyant tracer particles at different time intervals. Here $t = 0, 30, 60, 90s$

trajectory of the tracer particle is different to those expected of fluid elements, as it is observed, in figure 3.5, that the particles travel inwards towards the centre of a nearby vortex, highlighted by the increasing absence of tracer particles located in-between vortices as time progresses. However, after this initial transit, as seen in figure 3.2a, the tracers settle on a trajectory that is proper for a fluid parcel as stated by Babiano et al. (2000), where they travel hereafter in classical Euler flows as this one. This has been shown by the lack of radial motion by the tracer particles between $t = 60s$ and $t = 90s$. This principle applies to buoyant tracers also in chaotic and turbulent fluids. However, in areas of complex activity it is possible for buoyant particles to separate from this trajectory as is proper for a fluid parcel in search of another path.

3.5.3 Light

Finally a consideration of many light particles, as represented in figure 3.3. The light particles get drawn to the centre of rotating fluids due to the dominance of the material derivative in the general equation that acts like a pressure term. These particles were said trapped in vortex filaments by Biferale et al. (2005). As shown in figure 3.6, each tracer gets drawn towards the centre of the nearest vortex immediately, with

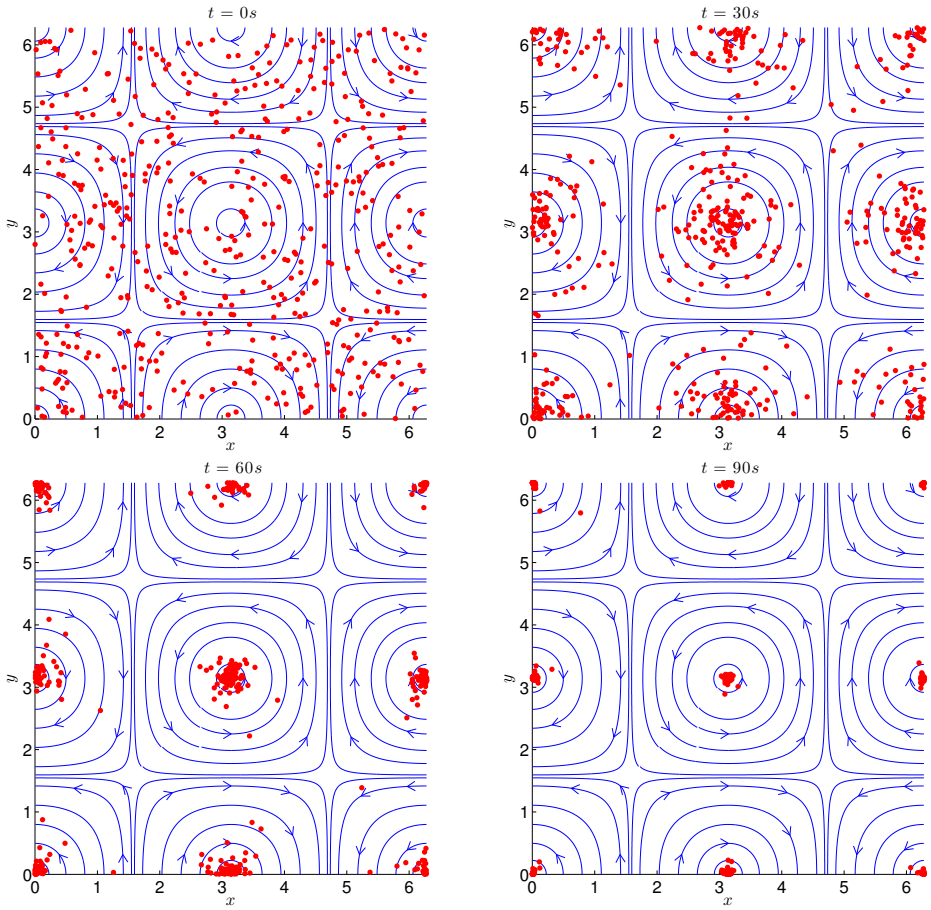

Figure 3.6: A plot showing the evolution of the position of light tracer particles at different time intervals. Here $t = 0, 10, 20, 30s$

the majority of tracers being trapped by $t = 90s$. This occurrence is also applicable to buoyant tracer particles (as shown in figure 3.2b) and is observed frequently. For example, the air bubbles that rest on the surface of a cup of coffee that is being stirred are seen to settle centrally.

Having considered the motion and trajectories of the different types of tracer, an attempt can be made to conclude these principles in a turbulent fluid.

Chapter 4

Characteristics of a Simulated Turbulent Fluid

This chapter shall outline the way in which the turbulent flow has been simulated numerically. This shall act as a prerequisite before the results of the previous chapter, concerning the trajectories taken by tracer particles submerged in Eulerien fluids, are applied to turbulence. Many methods of simulating turbulence numerically have been used recently, and the method in which this unpredictable nature is reproduced in this report lends much to the emergence of quantum turbulence. Although, as described by Paoletti et al. (2008), statistically there are differences separating quantum and classical turbulence, fluids simulated in this way are considered due to the current interest in velocity fields of this type, mainly concerning superfluids. This turbulent atmosphere is created by containing N discrete point vortices in an infinite, periodic box of two dimensions. This follows from the vortex filament method used to simulate quantum turbulence in three dimensions, Hänninen and Baggaley (2014), but taken in the x-y plane. Before proceeding, it is important to note several differences separating quantum and classical turbulence. As shown by Paoletti et al. (2008), classical turbulence follows near Guassian velocity statistics, whereas in quantum turbulence, the velocity statistics are strongly non-Gaussian in the tails of the distribution, seemingly following power law representations such that $\mathrm{PDF}(u_i) \propto u_i^{-3}$, where u_i denotes the velocity components u and v. Also, the study by Barenghi et al. (2014) presented the notion that each discrete vortex filament in quantum turbulence has fixed circulation, whereas classically it is seen that turbulent eddies possess continuous size and strength. Therefore, this model can be considered as the necessary framework supporting classical turbulence. Throughout this chapter, the position of a point vortex of positive circulation, that is $K_i = +k,\ k \in \mathbb{R}^+$, is denoted by a filled red circle, whereas the position of a point vortex of negative circulation, where $K_i = -k$ is denoted by a filled blue circle.

4.1 Two-Dimensional Vortex Points Model

Here the turbulent fluid defined by a system of two-dimensional point vortices is constructed. The velocity field induced by a vortex at position (x_j, y_j), of a model including N vortices alternating between positive and negative circulation of strength $\pm k$, is given

by

$$\mathbf{u}_f = (u, v), \tag{4.1}$$

where

$$u(x_j, y_j) = \sum_{\substack{i=1 \\ i \neq j}}^{N} \frac{-K_i(y_j - y_i)}{2\pi r_{ij}^2} \ , \ v(x_j, y_j) = \sum_{\substack{i=1 \\ i \neq j}}^{N} \frac{K_i(x_j - x_i)}{2\pi r_{ij}^2}, \tag{4.2}$$

and r_{ij} and K_i denote the distance separating vortices i, j, that is $r_{ij} = [(x_j - x_i)^2 + (y_j - y_i)^2]^{1/2}$, and the alternating circulation of the vortices, where $K_i = k(-1)^{i+1}$. The magnitude of the circulation, given by the line integral around the closed loop c, that defines the vortex line is given by

$$|K_i| = \left| \oint_c \mathbf{u}_f \cdot d\mathbf{l} \right|, \tag{4.3}$$

for a small line element $d\mathbf{l}$. The equation of motion for the fluid that models the trajectories of fluid elements, which in turn describes the motion of each vortex, is given by

$$\frac{dx_j}{dt} = u(x_j, y_j) \ , \ \frac{dy_j}{dt} = v(x_j, y_j). \tag{4.4}$$

Some preliminary tests will now be devised to validate as to whether the computation of this model acts correctly and imitates the expected trajectories of turbulent fluid elements.

4.1.1 Test: Vortex Pair

Firstly, consideration shall be given to the trajectory and velocity taken by a pair of vortices ($N = 2$), namely α and β of equal circulation, such that $K_\alpha = K_\beta = 1/10$. In considering the two-dimensional vortex points model, as stated by White et al. (2010), the magnitude of the velocity, at distance r, induced by a vortex is given by $k/2\pi r$. Relating this to the test, the vortex α will exert this velocity field onto vortex β and vice versa. This results in the vortex pair rotating anti-clockwise with velocity inversely proportional to $r_{\alpha\beta}$, that is the distance separating vortices α and β, given by

$$|\mathbf{u}_\alpha| = |\mathbf{u}_\beta| = \frac{K_\alpha}{2\pi r_{\alpha\beta}} = \frac{K_\beta}{2\pi r_{\alpha\beta}}. \tag{4.5}$$

This test is outlined as follows. Initially, the vortices α and β are placed at positions $(\pm 1/10, 0)$ as demonstrated in figure 4.1a. As $r_{\alpha\beta} = 1/5$, it is expected $|\mathbf{u}_\alpha| = |\mathbf{u}_\beta| = 1/4\pi$. To consider the results it is required that the magnitude of the velocity is calculated, which can be achieved in one of two ways. Either by considering the temporal periodicity of the wave-like curves in figure 4.1b, given by $\tau = 2\pi/\lambda$, where λ denotes the wavelengths of the curves corresponding to α and β. Or, by adapting the computation such that it stores each value of $u_\alpha, u_\beta, v_\alpha, v_\beta$ at discrete time intervals. Having used the latter, the magnitude of the velocity ($|\mathbf{u}_i| = (u_i^2 + v_i^2)^{1/2}$ for $i = \alpha, \beta$) is calculated in addition to the mean value of the magnitude of the velocity ($|\bar{\mathbf{u}}_i|$ for $i = \alpha, \beta$), using all data from the discrete time intervals. It can be seen that $|\bar{\mathbf{u}}_\alpha| = |\bar{\mathbf{u}}_\beta| \approx 0.0796$ with the vortices rotating around a fixed axis (the origin) in the anti-clockwise direction.

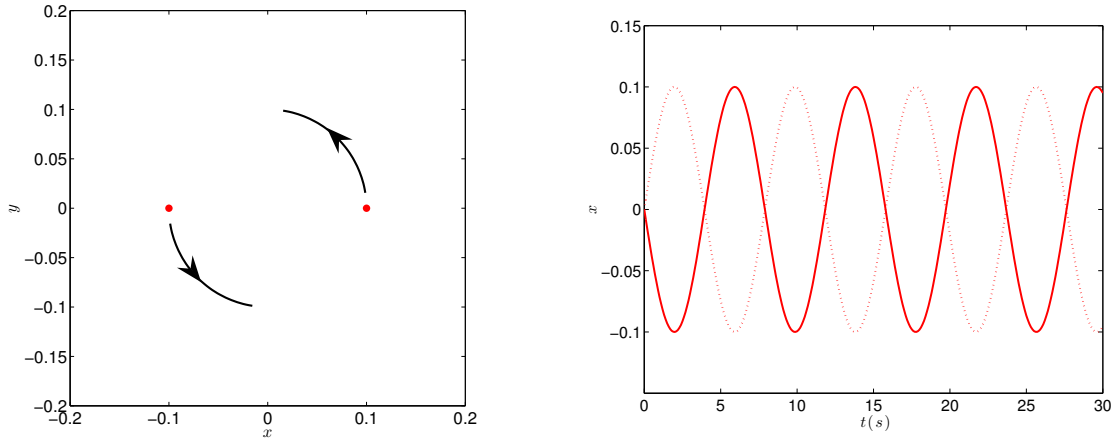

(a) (b)

Figure 4.1: (a) shows the initial set up of the particles, with arrows identifying the expected trajectories α (left) and β (right) take. (b) shows how the x co-ordinate of each vortex's position changes with time, the solid red line denotes α and the dashed red line denotes β.

The vortices maintained the distance separating the pair, with trajectories similar to those identified in figure 4.1a. This has been reinforced in figure 4.1b with the plot of the x co-ordinates of α and β against time, with the vortices appearing consistently in phase throughout. It follows that the percentage error in this test is 0.0034%. Also an identical test was carried out on the anti-vortex pair (where $K_\alpha = K_\beta = -1/10$). It resulted with the percentage error remaining the same, with the tracers rotating in the clockwise direction.

4.1.2 Test: Vortex- Anti-Vortex Pair

The trajectory and velocity of the vortex- anti-vortex pair are now examined. Again, remaining with $N = 2$ vortices, say ζ and η, but now of equal and opposite circulation, such that $K_\zeta = +1/10$ and $K_\eta = -1/10$. Using the same argument that was used for the vortex-pair, each vortex filament induces a velocity field of $k/2\pi r$, however, as shown in figure 4.2a, the opposite circulation of ζ and η shall assist in translating the pair with straight trajectories, normal to the line connecting ζ and η, with velocity

$$|\mathbf{u}_\zeta| = |\mathbf{u}_\eta| = \left|\frac{K_\zeta}{2\pi r_{\zeta\eta}}\right| = \left|\frac{K_\eta}{2\pi r_{\zeta\eta}}\right|. \tag{4.6}$$

Now for the conditions of the test. This time, ζ and η are placed at the co-ordinates $(0, \pm 1/20)$ respectively. In theory, these vortices should travel with translation velocity $|\mathbf{u}_\zeta| = |\mathbf{u}_\eta| = 1/2\pi$, because $r_{\zeta\eta} = 1/10$. As ζ, the vortex of positive circulation, is above η, the vortices are observed travelling in the positive x direction as highlighted by the plots of the positions of ζ and η at discrete time intervals in figure 4.2b. Having stored the velocity components of the test at each discrete time interval, it is found that the mean translation velocity (which in this case is also the magnitude of velocity) of each vortex is $\bar{u}_\zeta = \bar{u}_\eta \approx 0.1592$, resulting in a percentage error for this test being 0.0025%.

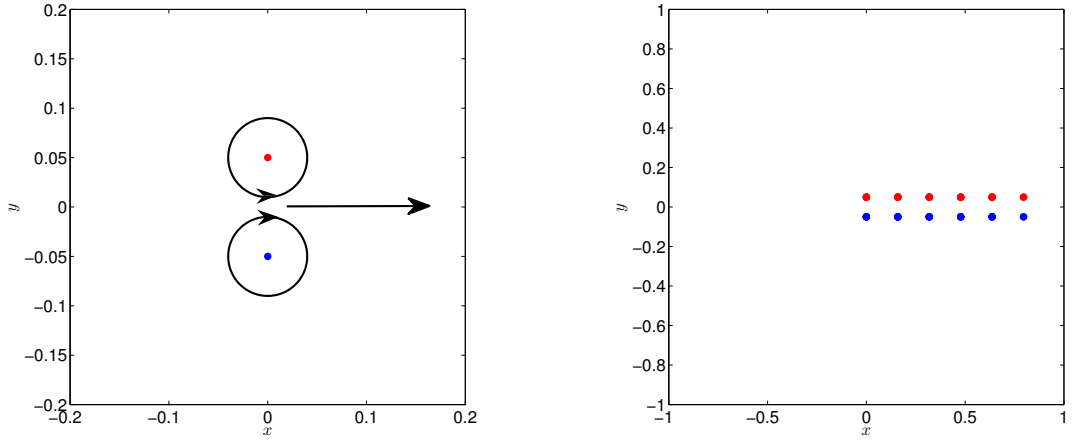

(a) (b)

Figure 4.2: (a) shows the initial set up of the test, with ζ above η and the direction of circulation has been highlighted. Black arrow shows the expected vortex trajectory. (b) shows the evolution of the position of ζ and η at t=0,1,2,3,4,5s respectively.

The similar computation to this test can now be checked, where the positions of the vortices are swapped, that is the vortex η is above ζ. The pair are seen moving in the negative x direction with the same average translation velocity as previously shown.

It can be noted that there is a correlation between the average percentage error in these tests and the distance separating the vortices, for instance the error associated with these calculations increases as the distance separating the vortices increases. However, consideration shall be given to simulations containing many vortices in a periodic box, using the same dimensions as to those shown in figure 4.2b, where the length of the square box, $L = 2\text{m}$. Values in which vortices are typically separated can be considered and it is possible to interpret how arbitrary distances can affect the validity of our results. First of all, the density of vortices, n, is defined as

$$n = \frac{N}{L^2}\text{m}^{-2}, \tag{4.7}$$

which shows an increase linearly as the total number of vortices, N, is increased, having previously fixed L. As N is increased, a decrease in the typical length that separates vortices, l, is observed. This typical length is given by

$$l = \frac{1}{\sqrt{n}}\text{m}. \tag{4.8}$$

In a typical simulation of this type, $N = 100$ vortices are considered in a box of $2\text{m} \times 2\text{m}$ dimensions, leading to $l = 1/5$ m. It can be established that vortex interactions that are separated by lengths that exceed l will not affect an arbitrary vortex in a significant way, as in all likelihood there will be some vortices within l that will greatly affect the trajectory and velocity of the vortex, due to the nature of the velocity field induced by a vortex. This statement implies that one should not consider the effects of vortices outside of the length scale l, as these vortices shall not impact on the validity of our results.

4.1.3 Test: Periodic Boundary Condition

Attention shall now be given to the effects upon implementing a periodic boundary condition into the developing computation. Prior to doing this, it is explained how this is achieved. The focus is on dealing with a confined space where the box is a two dimensional torus, and so the simulation will have to implement a condition in such a way that the points at the bottom of the box get affected by the points at the top of box as if next to them, and similarly with the other three edges. The method utilised to recreate this scenario involves creating 4 sets of ghost points identical to those considered, but placed to the north, south, east and west of the original box, separated by the length of the box, L as highlighted in figure 4.3a. In executing this condition, each ghost point must now also be summed over when computing the velocity components u_f and v_f. Implementing this condition means the net effect to each vortex from it's repeated ghost vortices is zero, yet vortices that are close to parallel boundaries are affected as if next to each other. An effective way to show this condition is as follows.

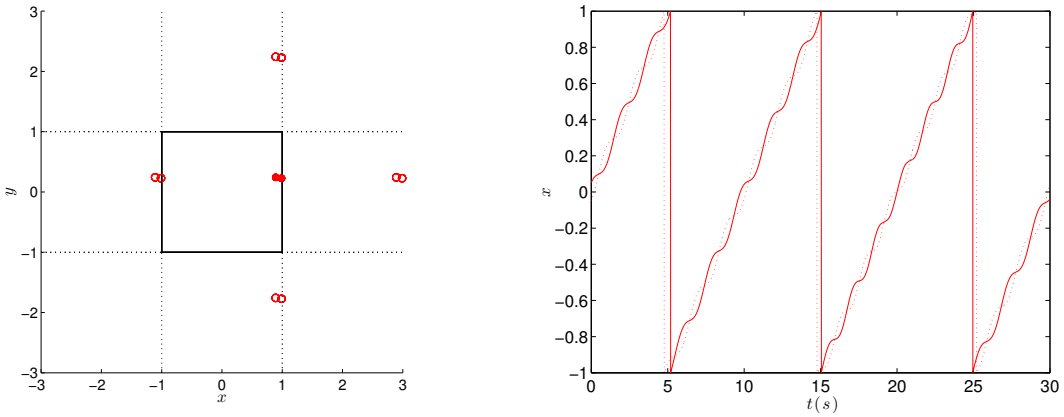

(a) (b)

Figure 4.3: (a) shows the orientation of the subject vortices (in the solid box) and ghost vortices (in the dotted boxes) at $t = 4.7s$, Ghost vortices are separated from the subject vortices by $L = 2$. (b) shows how the x co-ordinate of the vortices position changes with time.

Consider two vortices, of equal circulation that are positioned initially at $(\pm 1/20, 0)$, but now a uniform stream is added to the system, such that $\mathbf{U} = (U_x, U_y) = (1/5, 1/20)$. In implementing this condition, the equation modelling the trajectories of the vortices becomes

$$\frac{dx_j}{dt} = u_f(x_j, y_j) + U_x \ , \ \frac{dy_j}{dt} = v_f(x_j, y_j) + U_y. \tag{4.9}$$

This addition shall attract the vortices towards the right boundary of the box, making it possible to consider how the act of crossing this boundary affects the vortices . Examining figure 4.3b, it can be seen that as a vortex crosses a boundary, the distance separating the vortices changes greatly as expected. Despite this condition, the vortices remain in phase regardless of the distance separating them. In light of this, the average distance that separates the vortices, $\bar{r}_{ij}$ is calculated, disregarding times when $r_{ij} \approx L$.

Evaluating this quantity, it can be seen that in these times, $\bar{r}_{ij} \approx 0.0994$ yielding a percentage error of 0.6%. Thus, the conclusion is that implementing this periodic boundary should have no bearing on the validity of the results.

4.1.4 Further Considerations

Finally, a consideration that assists in streamlining computations can be discussed. Each point vortex shall be converted into a Rankine point vortex. The velocity field induced by a Rankine vortex, defined in polar co-ordinates is given by

$$\mathbf{u}_f = (u_r, u_\theta) = (0, u_\theta), \text{ where } u_\theta = \begin{cases} \frac{K_i r_{ij}}{2\pi a^2} \text{ if } r_{ij} < a \\ \frac{K_i}{2\pi r_{ij}} \text{ if } r_{ij} \geq a \end{cases}, \tag{4.10}$$

where the notation used previously is consistent here, and a is a constant. The Rankine acts identically to a regular vortex when $r_{ij} > a$. However, when $r_{ij} = a$, a maximum angular velocity is achieved, removing the singularity point as observed in a standard vortex. This control has been implemented to the velocity field to overcome issues when vortex pairs get too close to each other, and $|\mathbf{u}_f| \to \infty$ in these positions. In this case,

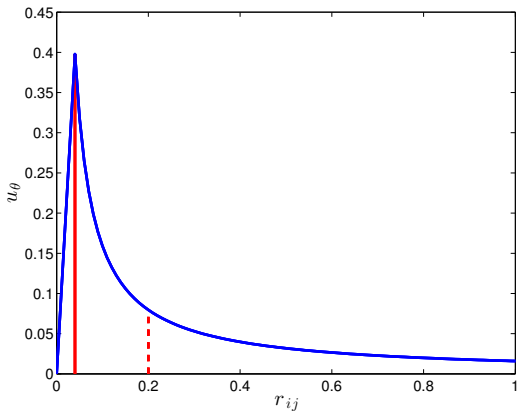

Figure 4.4: The velocity of each Rankine changes due to the distance separating a pair. Dashed red line shows the length scale l, being the average distance that separates a vortex, with the solid red line highlighting the choice of a.

the chosen time step, Δt, may be too large to catch up with the trajectory of the fast moving vortices, and variable time stepping methods would have to be introduced to ensure the results remain valid. As can be seen in the angular velocity profile given in figure 4.4, $a \ll l$ has been chosen, a convention applied so that there are still strong interactions between closely positioned vortices within the fluid, which assists in creating areas within the fluid familiar in classical turbulence. Before proceeding, the velocity field induced by the Rankine must be converted from polar to cartesian co-ordinates, which yields

$$\mathbf{u}_f = (u, v) = \begin{cases} \left(\frac{-K_i(y_j - y_i)}{2\pi a^2}, \frac{K_i(x_j - x_i)}{2\pi a^2}\right) \text{ if } r_{ij} \leq a \\ \left(\frac{-K_i(y_j - y_i)}{2\pi r_{ij}^2}, \frac{K_i(x_j - x_i)}{2\pi r_{ij}^2}\right) \text{ if } r_{ij} > a \end{cases}. \tag{4.11}$$

In implementing this convention, equations (4.1) and (4.2) have been amended accordingly.

4.2 Motion Statistics

In this section, an attempt shall be made to quantify the motion of the fluid elements, given by the velocity field produced by the vortex points model, when applying $N = 100$ vortices. This can be achieved by considering the velocity and acceleration probability density functions (PDFs), that are constructed by extracting the two components of velocity at discrete time intervals and constructing histograms, as considered by La Mantia et al. (2013) and Baggaley and Barenghi (2014).

4.2.1 Velocity

Firstly the velocity field induced by the discrete vortices is examined. The data generated by the velocity components of the vortices is normalised by dividing by the standard deviation of each sample and centred by subtracting the mean value, although in past literature this convention has not always been utilised, for example see Adachi and Tsubota (2011). Having constructed the PDFs for the normalised velocity components as shown in figure 4.5a, it can be seen that local to zero velocity, the data seems to follow Gaussian PDFs, given by

$$\mathrm{gPDF}(u_i) = \frac{1}{\sqrt{2\pi\sigma_i}} e^{\left(\frac{-(u_i-\bar{u}_i)^2}{2\sigma_i^2}\right)}, \tag{4.12}$$

where $\bar{u}_i$ represents the sample mean ($\bar{u}, \bar{v} \approx 0$) and σ_i represents the sample standard deviation for both components ($\sigma_u = 0.2922, \sigma_v = 0.3320$). However, as seen in the tails

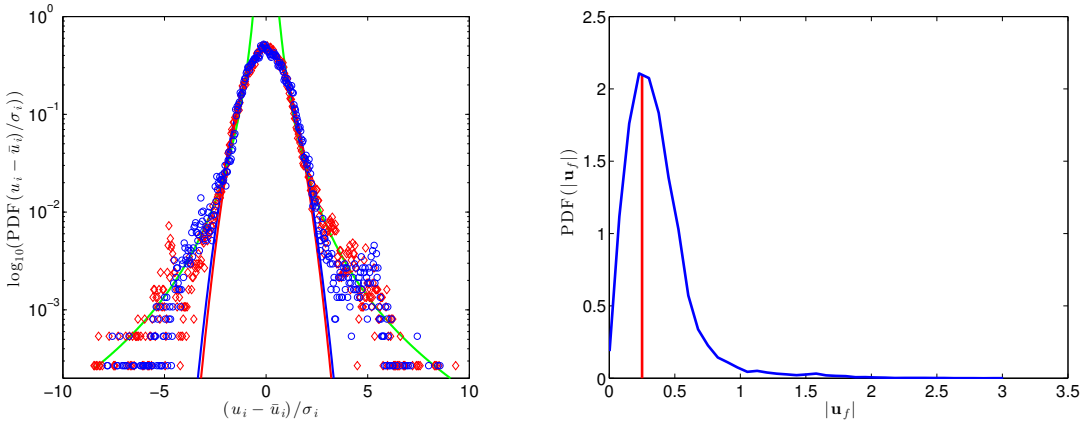

(a) (b)

Figure 4.5: In (a) there is the PDFs of the turbulent velocity components, the blue circles and red diamonds respectively show $u/\sigma_u, v/\sigma_v$. Blue and red solid lines show a Gaussian PDF fit for $u/\sigma_u, v/\sigma_v$ respectively. The green solid line highlights a power law fit for the turbulence. In (b) PDF of the magnitude of the velocity ($(u^2+v^2)^{1/2}$), where the red line highlights the 'characteristic velocity' $k/2l$. Both plots used the same data

of the distribution, there is deviance away from Gaussianity, where a power law best

fits the data. This is found such that $\mathrm{PDF}((u_i - \bar{u}_i)/\sigma_i) \propto ((u_i - \bar{u}_i)/\sigma_i)^{-3.2}$, consistent with the previous study of quantum turbulence.

In figure 4.5b, the PDF for the magnitude of the velocity, $|\mathbf{u}_f|$, has been constructed by taking the same data as used in figure 4.5a. Using this can assist in finding a value to denote τ_f, which shall be used later when considering the different tracer particles submerged in this turbulent fluid. Using this PDF, a characteristic velocity can be found for the fluid. This is estimated by $k/2l = 1/4$ ms^{-1}. Upon referencing back to equation (4.8), it was found that the typical length scale separating the fluid elements is $l = 1/5$ m, and consequently $\tau_f \approx 4/5$ s.

4.2.2 Acceleration

This procedure can now be repeated for the acceleration statistics of the fluid elements. Having stored the velocity components of the vortices at discrete time intervals as used previously, it is simple to compute the acceleration of these fluid elements using the high order forward finite difference method

$$\mathbf{a}_i^n = \frac{d\mathbf{v}_i^n}{dt} = \frac{-\mathbf{v}_i^{n-3} + 6\mathbf{v}_i^{n-2} - 18\mathbf{v}_i^{n-1} + 10\mathbf{v}_i^n + 3\mathbf{v}_i^{n+1}}{\Delta t}, \tag{4.13}$$

used by Baggaley and Barenghi (2014). In this study, they evaluated the acceleration component statistics in superfluids. The subscript denotes the i^{th} vortex and the superscript denotes the n^{th} time step. Figure 4.6a illustrates that the acceleration PDFs for the x and y components are identical, where the best power law fits have been found

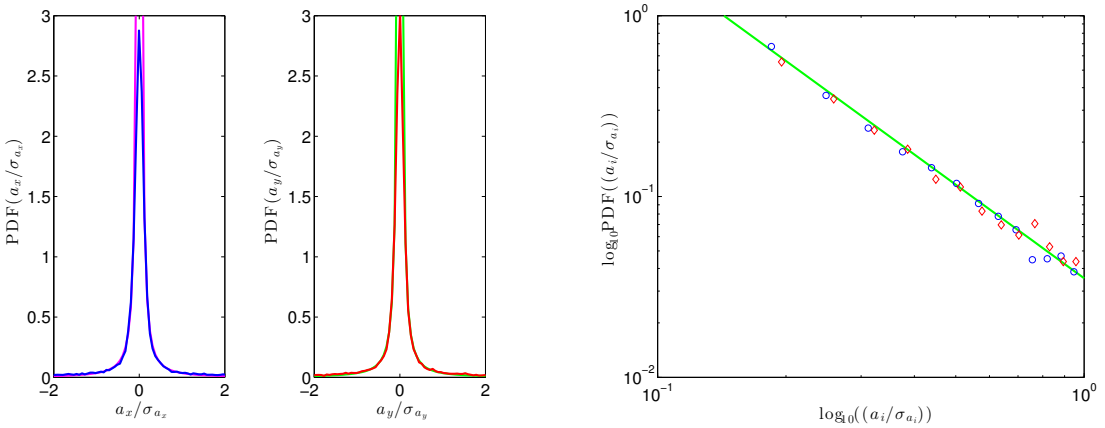

(a) (b)

Figure 4.6: In (a) we have a power-law representation of the PDF's for a_x (left) and a_y(right). In (b) we have PDF(a_x), PDF(a_y) plotted 'log log', to highlight the power law fit to both acceleration components, where blue circles and red diamonds respectively show a_x, a_y, superimposed over the power-law fit in green.

to be $\mathrm{PDF}(a_i/\sigma_{a_i}) \propto (a_i/\sigma_{a_i})^{-1.7}$, as highlighted by the pink and green lines for the x and y components of acceleration respectively. This is consistent with La Mantia et al. (2013) and has been highlighted in figure 4.6b, showing the suitability of the power law representation when the data is plotted on logarithmic scales, that acts in stretching the data.

Chapter 5

Tracer Particles in Turbulence

The results that have been evaluated throughout this report thus far will be applied to a current research area in this chapter. The behaviour of the different tracer particles, in which it was seen that heavy tracers preferentially concentrate, neutrally buoyant tracers eventually follow the streamlines of the fluid and light tracers get drawn into the centres of vortices, are now considered in a turbulent fluid, simulated as discussed previously in chapter 4.

Here, it shall be noted that the forthcoming figures that show the position of 500 tracer particles at different time intervals have been superimposed over the locally averaged vorticity, $\boldsymbol{\omega}$. This has been computed by splitting the box of $L = 2$m into a 100×100 grid and considering the influence of the local point vortices to each grid point. It follows that dark red regions within these figures correspond to $\boldsymbol{\omega} = +1$, dark blue regions correspond to $\boldsymbol{\omega} = -1$ and green regions correspond to $\boldsymbol{\omega} = 0$.

5.1 Heavy Particles

Firstly, consideration shall be given to the greatly researched area of heavy particles ($\rho_p = 10500\text{kgm}^{-3}$) suspended in turbulence. It was seen previously that the heavy particles sought areas of high vorticity or low strain. In this scenario, the inertia of the fluid is far greater than that of the particle, highlighted by the characteristic time of the fluid being far smaller than that of the particle, and so $St \gg 1$. This implies that the particle can not respond to sudden changes in fluid motion, and consequently, the particle acts far differently to typical fluid trajectories. This leads to the tracer particle settling in areas where the magnitude of vorticity is small, having previously escaped areas of greater vortex activity. This has been validated in figure 5.1 and the accompanying video, where the heavy particles constantly reattempt to position themselves into areas of locally low vorticity. As time progresses the population of particles in areas of locally low vorticity increases, with the only anomalies due to the fluid evolving into areas in which the heavy tracers are located at that particular snapshot of time. These particles do not react to this change in fluid velocity in this area, and so rather than following fluid streamlines, they instead get propelled away from these areas before being able to resettle where the vorticity is low. This can also be seen in the linked video, focus on the lower right quadrant to see the fluid evolving, and transporting the particles into green areas where there is zero vorticity. Here the

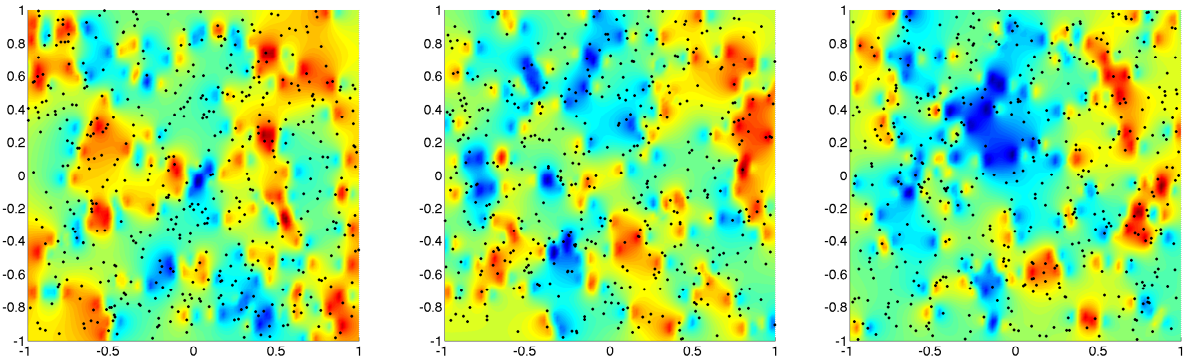

(a) (b) (c)

Figure 5.1: The position of the heavy tracer particles at time intervals (a) $t = 0s$, (b) $t = 5s$ and (c) $t = 10s$, superimposed over the local vorticity, $\boldsymbol{\omega}$. For the spatiotemporal evolution of the fluid and tracers find the video located at `https://www.youtube.com/watch?v=SRUj8i6wzys`.

particles attempt to settle, where the vorticity has dramatically reduced local to this area and the only way in which they shall move away from this location is if the turbulent flow evolves such that vortex interactions occur in this area.

5.2 Neutrally Buoyant Particles

Next, consideration shall be given to neutrally buoyant tracer particles ($\rho_p = \rho_f = 1000\text{kgm}^{-3}$). In chapter 3, it was concluded that the trajectories in which neutrally buoyant tracers can take are strictly not allowed by fluid parcels, as found by Babiano et al. (2000). In this case, the material derivative term in the general equation of motion for the tracers begins to influence their trajectory, and the expectation is that the particles get drawn towards vortices. From this some more characteristics of these

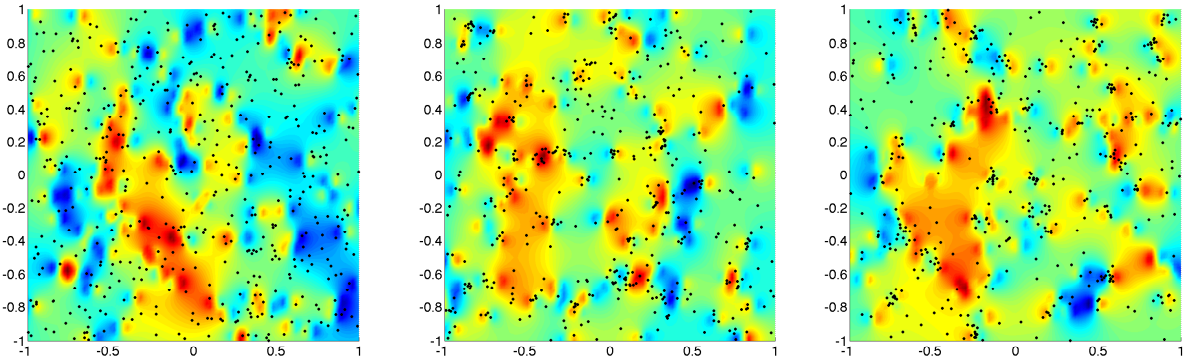

(a) (b) (c)

Figure 5.2: The position of the neutrally buoyant tracer particles at time intervals (a) $t = 0s$, (b) $t = 5s$ and (c) $t = 10s$, superimposed over the local vorticity, $\boldsymbol{\omega}$. For the spatiotemporal evolution of the fluid and tracers find the video located at `https://www.youtube.com/watch?v=KAvbgeCOq3M`.

tracers can be deduced. This is supported by work by Sergeev et al. (2006), in which they found that even in the relatively simple case of strategically placing 3 point vortices such that their trajectory was along a closed orbit, the trajectory of the particle is unstable. This leads to the assumption that in N point vortex systems, this instability is likely to be further reinforced by the chaotic nature. As seen in figure 5.2, the tracer particles get drawn towards areas of locally high vortex activity where the magnitude of vorticity is high, however, unlike in the case of light tracer particles (as shown in section 5.3), neutrally buoyant particles can rejoin the fluid streamlines after temporarily being trapped. Figure 5.2 and the linked video agrees with the conclusions of Babiano et al. (2000) and Sergeev et al. (2006). These conclusions are that the instability in particle trajectories seems to arrive due to the nature in which the particles can temporarily trap leading to seemingly chaotic behaviour. As highlighted in figure 5.3, where two

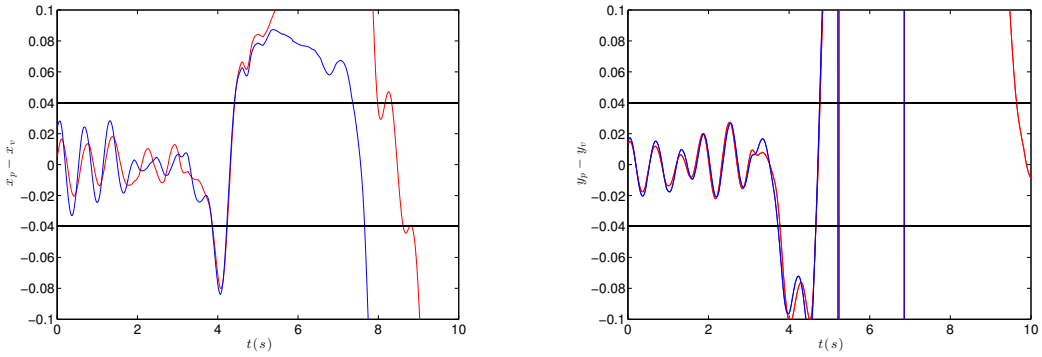

(a) (b)

Figure 5.3: The position of two trapped tracer particles with respect to a vortex as time progresses. (a) shows how the x co-ordinate of the particles deviates and (b) shows how the y co-ordinate of the particles deviates. x_p, y_p, x_v, y_v denote the x and y co-ordinate of the particle and vortex respectively. Black lines highlight the distance $\pm a$.

particles located between areas of positive and negative vorticity are considered, at initial position $(0.4, -0.2)$ approximately. This graph shows that temporarily a particle can be trapped within vortex trajectories, however, in comparison to the case of trapped light particles, neutrally buoyant particles act much more unpredictably. In fact, the particles possess the property to act against the force dragging them towards vortices and un-trap, rejoining the rest of the fluid, shown by the position of the tracers with respect to the vortex after $t = 4s$. This has also been shown in the accompanying video, where with the majority of tracers, the initial trajectory is seemingly towards an area of fluid containing a vortex, yet the tracer will not remain trapped hereafter. This chaotic nature of the fluid trajectory has caused a flurry of interest in recent years, with a range of techniques being used in an attempt to quantify this, for example, see the interest surrounding the trajectory curvature method as considered by Gupta et al. (2014).

5.3 Light Tracer Particles

Thirdly, consideration is given to the light tracer particles ($\rho_p = 1.2\text{kgm}^{-3}$). In chapter 3, it was seen that the light tracers trajectory was drawn towards the centres of vortices

before settling, which has been validated in this case of turbulence, and demonstrated by figure 5.4. As time progresses, the tracer particles appear trapped between local vortex

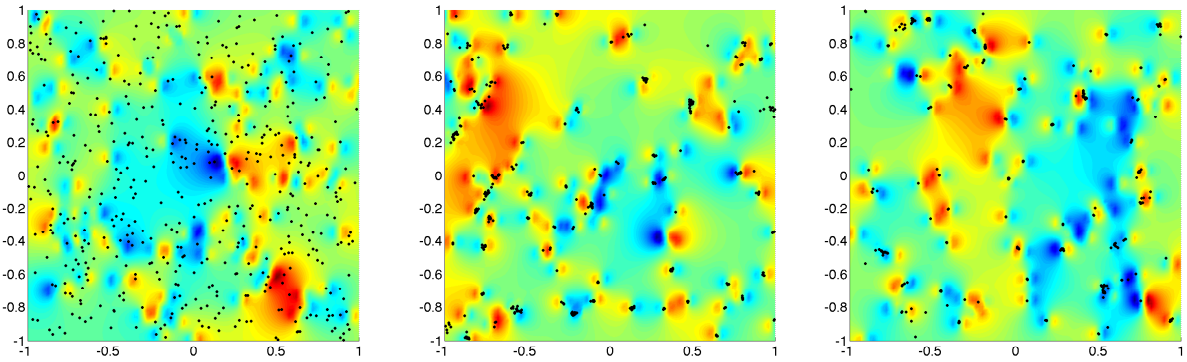

(a) (b) (c)

Figure 5.4: The position of the light tracer particles at time intervals (a) $t = 0s$, (b) $t = 5s$ and (c) $t = 10s$, superimposed over the local vorticity, $\boldsymbol{\omega}$. For the spatiotemporal evolution of the fluid and tracers find the video located at `https://www.youtube.com/watch?v=pWic9M5Nc38`.

trajectories. This is shown by the greater density of tracer particles in areas where the magnitude of vorticity is high (darker blue and red regions) or between areas of great difference between high and low vorticity, for example with reference to figure 5.4c, the region surrounding $(-0.6, -0.6)$ at $t = 10s$ can be observed, where several particles are located in-between areas of high vortex and high anti-vortex density. With reference to the approximate equation of motion for the light particle given by equation (3.4), it is seen that the material derivative term dominates, it attempts to drag the light tracers towards each vortex, yet is only successful in dragging the particle towards the closest vortex. In doing this, as the tracer gets drawn towards a vortex it settles, and there is nothing to suggest that the tracer could escape, consequently it must move with the vortex hereafter, trapped in its trajectory. This is shown in figure 5.5, where the

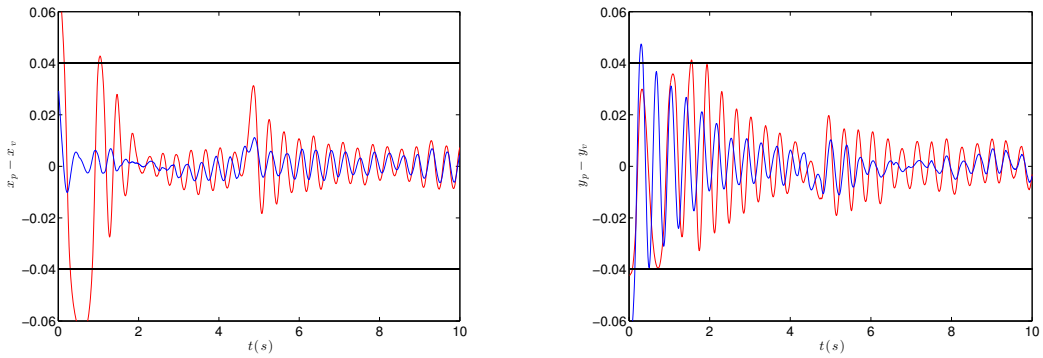

(a) (b)

Figure 5.5: The position of two trapped tracer particles with respect to a vortex as time progresses. (a) shows how the x co-ordinate of the particles deviates and (b) shows how the y co-ordinate of the particles deviates. x_p, y_p, x_v, y_v denote the x and y co-ordinate of the particle and vortex respectively. Black lines highlight the distance $\pm a$.

position of two tracer particles with respect to an arbitrary vortex has been illustrated (finishing at around $(-0.3, -0.9)$ at $t = 10s$, or at the end of the accompanying video). Both particles start initially outside the region where the Rankine condition comes into effect, and straight away the two tracers get drawn inside this radial distance. From here the particle is trapped within the vortex, and closely oscillates around the position of the moving vortex.

5.4 Motion Statistics

Finally this report shall interpret how the turbulent fluid exerts its velocity field onto each type of tracer particle. It was asserted in chapter 4 that the PDF of the fluids velocity field obeys a Gaussian PDF local to the sample mean, whereas in the tails a power law best represents the PDF. Now the response from this velocity field onto the tracer particle is examined. This is discussed by Bec et al. (2006), they presented results of direct numerical simulations of up to 120 million heavy tracers and discussed the impact of the Stokes' number in characterising the acceleration statistics of the tracer particles. They found that in using the simplified model that was introduced in chapter 3, the tails of the acceleration PDFs for the particles decrease in line with the Stokes' number. Although this report has proceeded in considering different characteristics, for example in the study of Bec et al. (2006), the geometry of the particles was changed to affect St and not the relative difference in density between the particle and fluid, and also, the trajectory in which different particles took was not considered. In light of this, the conjecture is formed such that as St decreases, the fluid can more easily pass its inertia onto the particle thus accelerating the particle will be far easier. With this, the variance in values in which the acceleration and velocity of the particle can take shall increase, therefore upon normalising these components (by dividing by the square root of the variance) the PDF of each of the components appears increasingly regulated. This notion shall assist in forming the assumption that as St decreases, the tails of the PDF for the normalised motion components shall also decrease, whist appearing more regular with fewer anomalies. This leads to the expectation that as St decreases, the PDF for the motion components shall appear flatter, because it is less likely for the particle to have zero velocity and acceleration. The method in which the PDFs have been constructed is identical to that of the fluid velocity components given by the vortex filament model. This has been achieved by storing the velocity components of each type of tracer at discrete time intervals and using this data to construct PDFs for the velocity and, using the finite difference method given by equation (4.12), the acceleration. It can be noted that the data used when constructing these statistics for each type of particle is consistent to the images and accompanying videos used previously in this chapter, and u_i represents the x and y velocity components u and v respectively and a_i represents the x and y components of the acceleration a_x and a_y respectively.

5.4.1 Heavy

In the case of the heavy particles, it is expected to observe a steep PDF for the velocity and acceleration components. The argument is as follows: it is harder to accelerate particles with large St, as they are unwilling to accept the inertia passed via the fluid

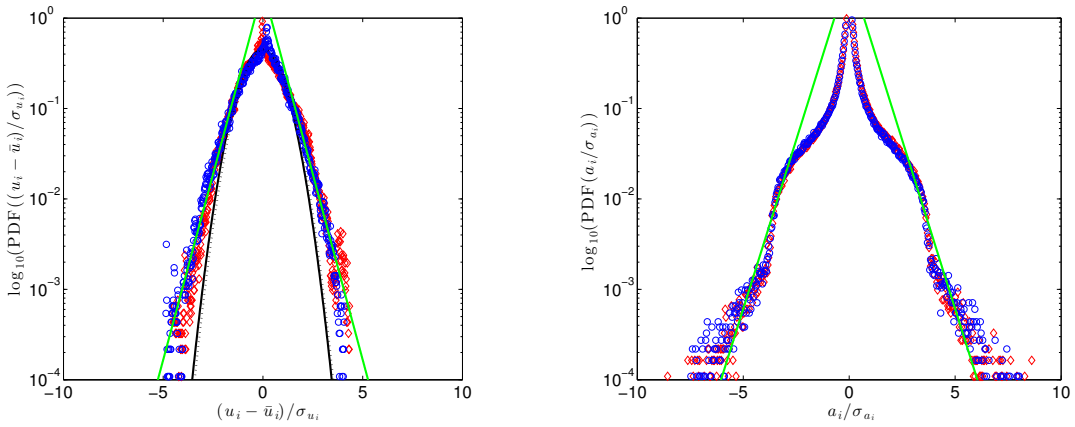

(a) (b)

Figure 5.6: $\log_{10}$(PDF)s for the normalised velocity components (a), and the normalised acceleration components (b) for heavy particles. u, a_x are denoted by red diamonds and v, a_y are denoted by blue circles in both figures.

velocity field. This means the PDF for the acceleration will be steeper in regions around zero where the particle has preferentially concentrated, with large tails due to the anomalies occurring when the particle gets propelled away from areas where the magnitude of vorticity is high. This argument has been validated in figure 5.6, where the normalised velocity components for the heavy particles' (centred by the mean $\bar{u}_i$, $\bar{u}, \bar{v} \approx 0$ and normalised by the standard deviation σ_{u_i}, $\sigma_u = 0.1454$, $\sigma_v = 0.1540$) PDF appears near-Gaussian, is highlighted by the solid and dashed black lines for the components of velocity u and v respectively. However, a better fit in the tails of the distribution as highlighted by the green line, seems to follow a distribution of the same family as the Gaussian, being the exponential distribution of form $\mathrm{PDF}((u_i-\bar{u}_i)/\sigma_{u_i}) \propto \exp(-1.9|(u_i-\bar{u}_i)/\sigma_{u_i}|)$. In addition, this figure also highlights the exponential fit for the PDF for the normalised acceleration components (where $\sigma_{a_x} = 2.6146$ and $\sigma_{a_y} = 2.6288$), where it has been shown the best fit for the PDF in the tails follows $\mathrm{PDF}(a_i/\sigma_{a_i}) \propto \exp(-1.7|a_i/\sigma_{a_i}|)$.

5.4.2 Neutrally Buoyant

As previously discussed, the buoyant particles can take trajectories which fluid parcels can not, but will eventual settle into the streamlines of the fluid regardless of the chaotic nature of its trajectory. Due to this difference in trajectory, it is expected that the PDF of the motion statistics of the tracer particles shall vary compared to the PDF of the fluid motion statistics, being near Gaussian as frequently observed in classical turbulence. Figure 5.7 highlights these claims, where the normalised velocity components of the buoyant tracer particles' (again centred by the mean $\bar{u}_i, \bar{u}, \bar{v} \approx 0$ and normalised by the standard deviation $\sigma_{u_i}, \sigma_u = 0.2587, \sigma_v = 0.2793$) PDF appears considerably more Gaussian compared to that given by heavy particles. The is due to a greater spread of data assisting in a more consistent fit when normalised to the Gaussian PDFs plotted by the solid and dashed black lines for the components of velocity u and

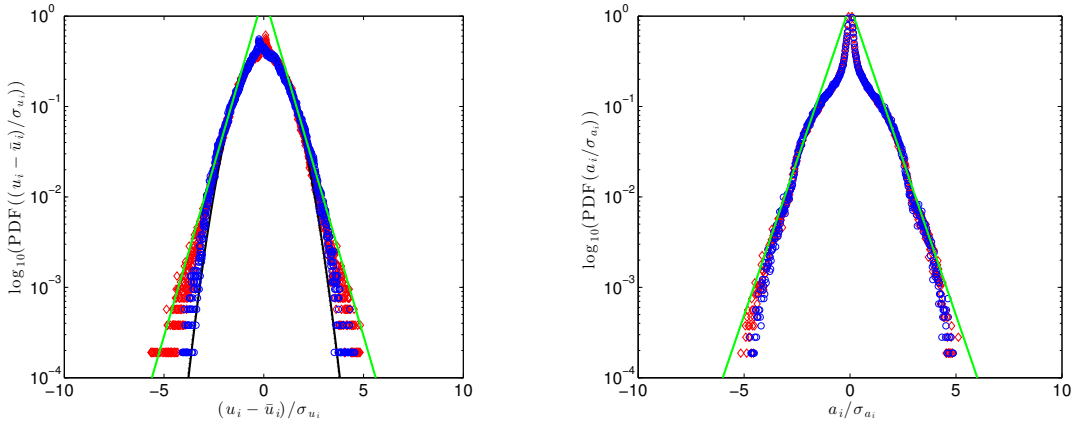

(a) (b)

Figure 5.7: $\log_{10}$(PDF)s for the normalised velocity components (a), and the normalised acceleration components (b) for buoyant particles. u, a_x are denoted by red diamonds and v, a_y are denoted by blue circles in both figures.

v respectively. However, there still remains a deviance away from strict Gaussianity, where a better representation in the tails is again given by an exponential distribution of the form $\mathrm{PDF}((u_i - \bar{u}_i)/\sigma_{u_i}) \propto \exp(-1.7|(u_i - \bar{u}_i)/\sigma_{u_i}|)$. This is highlighted by the green line in figure 5.7a. Moving onto the normalised acceleration components (where $\sigma_{a_x} = 176.4570$ and $\sigma_{a_y} = 181.3984$), it is noted that another exponential distribution best fits the tails of the distribution such that $\mathrm{PDF}(a_i/\sigma_{a_i}) \propto \exp(-1.6|a_i/\sigma_{a_i}|)$ as highlighted in figure 5.7b by the green line.

5.4.3 Light

Having previously considered the trajectory in which light particles undertake, it has been shown that these tracers get drawn to the nearest discrete vortex before being trapped hereafter which has been highlighted by the vast density of tracers in regions of high vortex interaction, back in figure 5.4. In light of this, an argument can be formed to believe that the motion PDFs of the light tracer shall be consistent to that of the fluid it is suspended in. However, as shown in the accompanying video, the light tracers do not solely get drawn to single vortices, but many get drawn towards areas of high vortex interaction. Thus, the net activity of the particles' motion may be close to zero due to the velocity field induced by multiple vortices cancelling out to zero. This will thereby reduce any tails of the PDF believed to be present. Also, due to the $St \ll 1$ for the light particle, the fluid can easily transport its inertial onto the tracer, which shall lead to a flatter acceleration PDF. This means it becomes less likely for there to be zero acceleration. As shown in figure 5.8, it has been shown that the normalised velocity PDF ($\bar{u}, \bar{v} \approx 0, \sigma_u = 0.3117, \sigma_v = 0.3086$) is near Gaussian as highlighted by the solid and dashed black lines for the components u, v respectively. However a closer fit in the tails is highlighted by the exponential distribution (green line) which is given by $\mathrm{PDF}((u_i - \bar{u}_i)/\sigma_{u_i}) \propto \exp(-1.6|(u_i - \bar{u}_i)/\sigma_{u_i}|)$ where the tail appears linear when plotted semi-logarithmically. The normalised acceleration PDF ($\sigma_{a_x} = 526.0563, \sigma_{a_y} =$

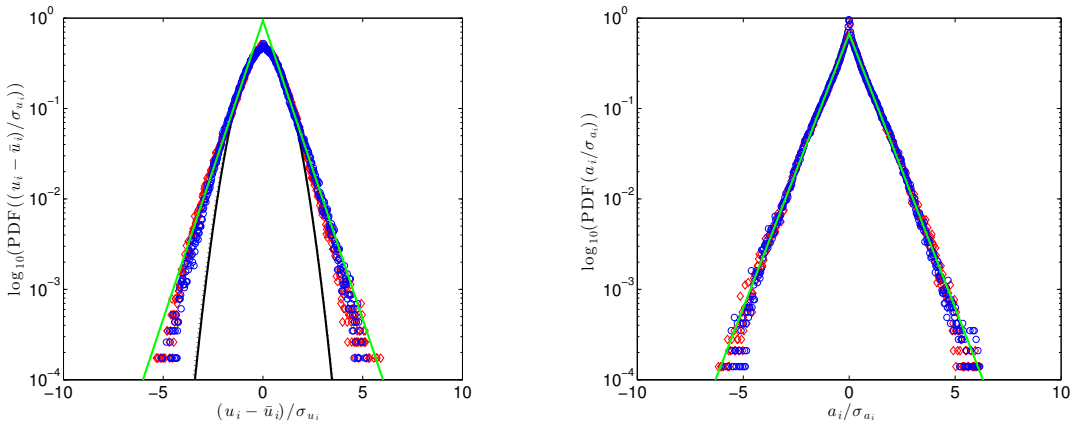

(a) (b)

Figure 5.8: $\log_{10}$(PDF)s for the normalised velocity components (a), and the normalised acceleration components (b) for light particles. u, a_x are denoted by red diamonds and v, a_y are denoted by blue circles in both figures.

523.4222), has shown that an exponentially distribution can model the entirety of the data set. This is due to the standard deviation being incredibly large for this case, where the light particles are able to travel with fluid elements and respond to any sudden change in direction and velocity. Thus upon normalising this quantity there appears a linear relationship between the PDF and modulus of the normalised acceleration when plotted semi-logarithmically, of the form $\mathrm{PDF}(a_i/\sigma_{a_i}) \propto \exp\left(-1.4|a_i/\sigma_{a_i}|\right)$, highlighted by the green solid line in figure 5.8b.

Chapter 6

Conclusion

This report attempted to quantify and discuss the characteristics behind the motion of different tracer particles in turbulence and build upon previous academic resources. Throughout, the fundamentals of particle tracing have been heavily evaluated, where the equation of motion for a small spherical tracer particle has been derived along with the relevant and necessary assumptions.

In addition to this this report has reinforced previous academic work. It has been shown that in two-dimensional, simple Eulerien fluids that different particles can be categorised. Having provided the results of direct numerical simulations, it has been observed that heavy particles preferentially concentrate in areas of low vorticity or high strain, neutrally buoyant particles act chaotically and posses the innate ability to partake in trajectories that fluid elements simple cannot, and that light particles get trapped within vortex trajectories.

From here, a way in which to simulate a turbulent fluid was discussed. Although the method utilised, the vortex points model, does not possess the continuous nature of turbulent eddies as observed experimentally on universal scales, it provides the necessary framework to support classical turbulence. Such as the work of Küchemann, in which he stated "vortices are the sinews and muscles of fluid motions" (Hänninen and Baggaley (2014)). Using this model, which lends much of derivation to the characteristics of quantum turbulence, the results of La Mantia et al. (2013) have been validated, where the PDFs of velocity and acceleration components have been proved to differ from those of classical turbulence Paoletti et al. (2008). It has been shown that the tails of both the normalised velocity and acceleration PDFs for x and y components follow power law representations, where $\mathrm{PDF}(v_i/\sigma_{v_i}) \propto |v_i/\sigma_{v_i}|^{-3.2}$ and $\mathrm{PDF}(a_i/\sigma_{a_i}) \propto |a_i/\sigma_{a_i}|^{-1.6}$.

These fundamentals of the trajectories of different tracer particles in the mathematically viable Eulerien fluids and the method in which turbulence can be simulated have been combined to yield the current hot topic of modern day fluid dynamics. From this two conclusions have been made. Firstly, the trajectories of the different tracers in turbulence have remained consistent to their Eulerien counterparts. This is illustrated by the plots of the sedimentation of the tracer particles at different snapshots in time, and also the motion of the tracer particles provided in the linked videos. Secondly, the PDF of the tracer particles changes due to the particles St. It has been observed, that the PDFs for the velocity of the particles remains near-Gaussian, as observed in experiments classically. However, a better fit for the tails of the PDF can be made by

considering a distribution of the same family to that of the Gaussian, being the exponential distribution. It has been shown that as St increases, the exponential fit of the distribution steepens. This is because the particle becomes less responsive to the motion exerted by the fluid, and it becomes increasingly likely that the particle will possess no velocity as opposed to responsive particles of small St. Finally, the acceleration PDF for each tracer has been considered, where it has been found that the variance of values in which the acceleration can take increases as St decreases. This conclusion arises due to the particle of smaller St being able to respond immediately to changes in fluid motion, and in this turbulent scenario, the change in the velocity of the particle induced by the chaotic nature of the carrier fluid can take large values. As this variance increases with St, upon normalising the acceleration component, the acceleration PDF appears regulated where an exponential distribution can again be used to best describe the nature of the PDF. As consistent with the velocity PDF, as St increases, the exponential fit of the distribution steepens.

Although this research area still lacks the maturity and clarity of other disciplines of modern applied mathematics due to it's inherent chaotic nature, within the past 20 years there have been significant strides forward that build on the pioneering work of Kolmogorov with the use of mathematical and experimental tracers. As modern day fluid dynamics takes this path, further work in this area will be surrounding the geometry of the trajectory that buoyant and heavy tracer particles can take in three-dimensions upon changes in St, created by changing the size of the tracer. The author believes that upon considering this direction of study, greater descriptions of the nature of the trajectories in which tracer particles induced by the velocity fields of the turbulent fluids can be formed. Under infinitesimally small St, it is widely known that buoyant and heavy tracer particles take trajectories incredibly close to the streamlines of turbulent fluids. Upon considering this trajectory using the curvature method of Gupta et al. (2014), wider applications of impurities in turbulent flows could begin to be classified. With this greater understanding and the utilisation of modern methods, it may be possible to describe our surroundings in greater depth, whether that's the issues of dust interrupting the efficiency of modern day car engines or the transport of pollution in the atmosphere.

Acknowledgements

The author wishes to thank his supervisor Prof. Carlo Barenghi for providing intellectual input and help, prompting fruitful discussion and assisting in finding the direction of study throughout this project.

Bibliography

H. Adachi and M. Tsubota. Numerical study of velocity statistics in steady counterflow quantum turbulence. *Phys. Rev. B*, 83:503, 2011.

A. Babiano, J. Cartwright, P. Oreste, and A. Provenzale. Dynamics of a small neutrally buoyant sphere in a fluid and targeting in hamiltonian systems. *Phys. Rev. Lett.*, 84: 5764, 2000.

A. Baggaley and C. Barenghi. Acceleration statistics in thermally driven superfluid turbulence. *Phys. Rev. E*, 89:033006, 2014.

C. Barenghi, L. Skrbek, and K. Sreenivasan. Introduction to quantum turbulence. *PNAS*, 111:4647, 2014.

J. Bec, L. Biferale, G. Boffetta, A. Celani, M. Cencini, A. Lanotte, S. Musacchio, and F. Toschi. Acceleration statistics of heavy particles in turbulence. *Journal of Fluid Mechanics*, 550:349, 2006.

L. Biferale, G. Boffetta, A. Celani, A. Lanotte, and F. Toschi. Particle trapping in three-dimensional fully developed turbulence. *Physics of Fluids*, 17:701, 2005.

W. Cheney and D. Kincaid. *Numerical Mathematics and Computing*. Thomson Brooks/Cole, 2008.

A. Gupta, D. Mitra, P. Perlekar, and R. Pandit. Statistical properties of the intrinsic geometry of heavy-particle trajectories in two-dimensional, homogeneous, isotropic turbulence. *arXiv: 1402.7058v1*, 2014.

R. Hänninen and A. Baggaley. Vortex filament method as a tool for computational visualisation of quantum turbulence. *PNAS*, 111:4667, 2014.

M. La Mantia, D. Duda, M. Rotter, and L. Skrbek. Lagrangian accelerations of particles in superfluid turbulence. *Journal of Fluid Mechanics*, 717, 2013.

M. Maxey and J.Riley. Equation of motion for a small rigid sphere in a nonuniform flow. *Physics of Fluids*, 26:883, 1983.

R. Maxey. The gravitational settling of aerosol particles in homogeneous turbulence and random flow fields. *Journal of Fluid Mechanics*, 174:441, 1987.

R. Monchaux, M. Bourgoin, and A. Cartellier. Preferential concentration of heavy particles: A voronoi analysis. *Physics of Fluids*, 22:304, 2010.

M. Paoletti, M. Fisher, K. Sreenivasan, and D. Lathrop. Velocity statisitcs distinguish quantum turbulence from classical turbulence. *Phys. Rev. Lett.*, 101:501, 2008.

D. Poole, C. Barenghi, Y. Sergeev, and W. Vinen. Motion of tracer particles in He II. *Physical Review B*, 71:514, 2005.

E. Saw, A. Shaw, S. Ayyalasomayajula, P. Chuang, and A. Gylfason. Inertial clustering of particles in high-reynolds-number turbulence. *Phys. Rev. Lett.*, 100:214501, 2008.

Y. Sergeev, C. Barenghi, D. Kivotides, and W. Vinen. Instability of trajectories of solid particles around vortex lines. *Physical Review B*, 73:502, 2006.

K. Squires and J. Eaton. Preferential concentration of particles by turbulence. *Physics of Fluids A: Fluid Dynamics*, 3:1169, 1991.

A. White, C. Barenghi, N. Proukakis, A. Youd, and D. Wacks. Nonclassical velocity statistics in a turbulent atomic bose-einstein condensate. *Phys. Rev. Lett.*, 104:301, 2010.